

**NOVEL, MINIATURE MULTI-HOLE PROBES AND  
HIGH-ACCURACY CALIBRATION ALGORITHMS  
FOR THEIR USE IN COMPRESSIBLE FLOWFIELDS**

*by*

***Othon K. Rediniotis, Ph.D.***  
*Aerospace Engineering Department*  
*Texas A&M University*  
*College Station, Texas*

*Final report for the research supported by NASA Langley,  
Flow Modeling and Control Branch,  
Mr. William Sellers monitor,  
under grant NAG-1-1753.*

*College Station, July 1999*



## GENERAL

This is the final report for a three-year grant with the Flow Modeling and Control Branch at NASA Langley. Mr. William Sellers was the technical monitor for the project. The effort actually consisted of three one-year projects with the following titles:

*First year: "Application of Artificial Neural Networks to the Calibration of the 5-Hole Probe"*

*Second year: "Extension of the Neural Network Probe Calibration Code, PROBENET, to various shapes of 5- and 7-Hole Probes and Reynolds Number Effects".*

*Third Year: "Extension of the Multi-Hole-Probe Measurement Capabilities to High-Shear and Near-Wall Flows".*

Annual reports at the end of each year were also submitted. The title and the contents of the present report are such that they summarize the results of the three-year effort.

Two new calibration algorithms were developed for the calibration of non-nulling multi-hole probes in compressible, subsonic flowfields. The reduction algorithms are robust and able to reduce data from any multi-hole probe inserted into any subsonic flowfield to generate very accurate predictions of the velocity vector, flow direction, total pressure and static pressure. One of the algorithms PROBENET is based on the theory of neural networks, while the other is of a more conventional nature (polynomial approximation technique) and introduces a novel idea of local least-squares fits. Both algorithms have been developed to complete, user-friendly software packages.

New technology was developed for the fabrication of miniature multi-hole probes, with probe tip diameters all the way down to 0.035". Several miniature 5- and 7-hole probes, with different probe tip geometries (hemispherical, conical, faceted) and different overall shapes (straight, cobra, elbow probes) were fabricated, calibrated and tested. Emphasis was placed on the development of four stainless-steel conical 7-hole probes, 1/16" in diameter calibrated at NASA Langley for the entire subsonic regime. The developed calibration algorithms were extensively tested with these probes demonstrating excellent prediction capabilities. The probes were used in the "trap wing" wind tunnel tests in the 14'x22' wind tunnel at NASA Langley, providing valuable information on the flowfield over the wing.

This report is organized in the following fashion. It consists of a "Technical Achievements" section that summarizes the major achievements, followed by an assembly of journal articles that were produced from this project and ends with two manuals for the two probe calibration algorithms developed.



## **TECHNICAL ACHIEVEMENTS**

The multi-hole pressure probe is a cost effective, robust and accurate instrument for three-dimensional velocity and pressure measurements in a wide range of flowfields. For steady-state measurements, 5- and 7-hole probes are capable of resolving flow angularities up to approximately 75 degrees and predict the flow conditions with high accuracy. Although powerful, measurement techniques such as Laser Doppler Velocimetry (LDV) and Particle Image Velocimetry (PIV) have a number of disadvantages compared to multi-hole probes. LDV and PIV require the use of costly components, such as expensive lasers and optical equipment. Both methods are complex and require painstaking alignment of lasers and optical equipment to obtain accurate flow measurements, and it is often hard to get good results outside the laboratory environment.

Since multi-hole pressure probes are intrusive flow-diagnostics instruments, concerns of probe interference with the flows it is trying to measure always arise. For example, in the case of leading-edge vortical flows over delta wings, the presence of the probe in the neighborhood of the vortex core can induce premature vortex breakdown<sup>1</sup>. Therefore, a strong incentive exists to reduce the probe size, thus reducing the interference. Concurrently, probe size reduction offers higher spatial resolution, for measurements in high-shear flows. Also, when measuring near a surface, a distance of at least four probe diameters should be maintained in order to avoid wall effects. Smaller probes can measure closer to the surface without violating this proximity rule. However, probe size reduction presents fabrication as well as frequency response challenges. In terms of fabrication, probe tip surface quality is important in measurement accuracy. For two different calibration surfaces, the smoother surface typically yields higher prediction accuracies. This is self-evident if one considers the fact that typical interpolation techniques use smooth continuous functions to locally model the calibration surface. The smoothness of the calibration surface depends, in turn, on the tip surface quality. Maintaining the same relative tip surface roughness (average tip surface imperfection size divided by the probe diameter) becomes a fabrication challenge as the probe diameter decreases. For the present work we were able to reduce the probe diameter to as low as 0.035", maintaining the same high surface quality of typical 0.125" diameter probes. Details on these technical developments are given in our journal article in Appendix A.

In a different challenge, as the probe diameter decreases, the tubing frequency response decreases. We have developed a simple technique to correct for the pressure measurement error produced in miniature multi-hole pressure probes due to the lag in the response of the probe tubing system. As the size of the pressure probe is reduced in order to reduce flow disturbance, the probe's frequency response deteriorates. Reduced frequency response generally causes the "wait" times in flow-mapping experiments to increase. The "wait" time is the time that the probe, after it moves to a new measurement location in the flow field, has to wait before data-acquisition can be performed, in order for the pressures at the probe pressure transducers to reach steady state. Moreover, deterioration of probe frequency response limits its capability to resolve temporal information in unsteady flows. In the present work we introduce a simple algorithm that significantly improves a probe's frequency response. Detailed work in the area was carried out by Whitmore<sup>2</sup>. He developed a mathematical model for a tubing system, derived from the Navier-Stokes and continuity equations. Based on this model, he then developed an algorithm to compensate for pneumatic distortion. The technique presented here is simpler, much less computationally intensive and



is thus amenable to real-time implementation. It should, however, be pointed out that the technique presented herein is applicable only to critically-damped or over-damped tubing systems, as discussed in the accompanying publication. Details on the developed technique are given in our journal article in Appendix B.

Probe calibration is generally performed by placing the probe in a flowfield with known velocity magnitude and direction. The probe is pitched and yawed (or coned and rolled) through a range of angles, to cover the range of possible velocity vector orientations. For each probe orientation the pressures from the five (or seven) pressure ports are recorded. This procedure is typically performed for angle increments of 2 to 5 degrees, resulting in approximately 1000 to 3000 discrete calibration points, for a cone angle range of 0° to 75° and the entire roll angle range (0° to 360°).

After the probe has been calibrated it can be used to measure the flow properties in an unknown flowfield. By measuring the probe port pressures at a point and “comparing” them to the calibration data, estimates of the flow angles and the velocity magnitude can be made. This “comparison” process is achieved by the calibration algorithm. In the present work, a neural network based calibration algorithm was successfully developed. Artificial neural networks have been effectively applied to mechanical and control systems. In aerodynamics, networks have proven their worthiness both as installed components in the aircraft control systems as well as research tools to investigate, model and control fluid flows<sup>3-5</sup>. Neural networks were coupled with flow measurement tools such as an omni-directional pressure probe to investigate separated and recirculating flows<sup>6</sup>. In the present work, a novel neural network calibration scheme has been formulated for use in the calibration of multi-hole pressure probes (5-hole or 7-hole). This procedure utilizes a large database of calibration information taken over a large range of flow cone angles (up to 75 degrees). The calibration data is then used to train a multi-layer neural network to predict the flow variables based on calculated pressure coefficients. During the training process, a Network Information file is generated that contains the necessary details of the network weights and biases. Subsequently, test data presented to the network is processed in a feedforward mode to predict the flow direction and magnitude based on the network’s knowledge. This versatile technique allows for non-uniform calibration grids, dense calibration grids and updating of the calibration data, provides high prediction accuracy and is very fast in the feedforward mode. Also, the speed in the feedforward mode is independent of the size of the calibration file in contrast to conventional local interpolation algorithms<sup>6,7</sup> of similar accuracy, whose speed is highly dependent on the size of the calibration data file. Moreover, the size of the feedforward code is on the order of a hundred lines, rendering interfacing with existing user codes (such as data-acquisition and data post-processing codes) extremely easy.

Researchers in the flight-test community have used the principles of multi-hole probes to develop flush air data systems<sup>8-11</sup>. In these systems, the nose of the aircraft is instrumented with multiple pressure ports, strategically positioned, and in essence operates as a giant multi-hole probe. In some efforts, neural networks have been successfully used, even in real-time, to extract air data information from the pressure measurements<sup>12</sup>, with speeds similar to the algorithm presented here. These air data systems have a different port arrangement than typical 5 and 7-hole probes, a higher number of ports and are not plagued by calibration issues that emerge as a result of miniaturization. Such an issue for example is the transportability of the calibration from one system to another. For the miniature probes discussed here, calibration transportability, without compromising measurement accuracy, is not an option



and each probe has to be calibrated individually. This is due to the fact that the effect of the probe manufacturing defects on the calibration is inversely proportional to the size of the probe. Details on our novel neural network algorithm are given in our journal paper in Appendix A.

In a different approach, a different probe calibration algorithm was developed, employing regional polynomial fit and local least-squares (LLS) calibration data point interpolation. Using only a few selected calibration data points that have similar angle coefficients as the measured angle coefficients, a low-order polynomial fit is created. The calibrated probe can be inserted into an unknown flowfield and the port pressures from the probe are recorded and compared with the port pressures in the calibration file through a set of non-dimensional pressure coefficients. When the  $N$  most similar pressure signatures are located in the calibration database, four low order least squares polynomials (for the two flow angles and the total and static pressure coefficients) are created using those data points in the calibration database. Using these polynomials, the two flow angles and the total and static pressure coefficients, for the test point, are determined. From the total and static pressure coefficients the local total and static pressures are determined. The predicted angles of the flow are relative to the probe coordinate system. To get the angles relative to the test area coordinate system a simple transformation is performed using the probe mounting geometry. The velocity magnitude and Mach number are calculated from the total and static pressure coefficients using adiabatic, perfect gas laws. It should be noted here that knowledge of the local total temperature is also required; however for the flows of interest here the total temperature is approximately constant and equal to the free-stream total temperature which is measured and known. Thus the velocity vector, both magnitude and direction can be found for any unknown subsonic flowfield. Four miniature 7-hole probes were designed and built. They were subsequently calibrated at the NASA Langley Flow Modeling and Control Branch. Details on the developed hardware and software described above are given in our under-review journal paper in Appendix C. The work describes the calibration and data reduction procedures, Mach and Reynolds number effects on the calibration and a detailed uncertainty analysis. Some important results are summarized below.

The non-dimensional angle and pressure coefficients used internally in the data reduction algorithm have an almost negligible dependence on Reynolds number and a more pronounced dependence on Mach number. A test point at a certain Mach and Reynolds number can be reduced with calibration data taken at completely different Mach and Reynolds numbers and still predict the velocity vector, both magnitude and direction with reasonable accuracy. However reducing test data with a calibration file at the same Mach and Reynolds number will yield the most accurate predictions. Thus to obtain high prediction accuracy throughout the entire subsonic regime, it is necessary to calibrate the probe at a wide range of Mach and Reynolds number.

An uncertainty analysis of the 7-hole probe measurements was performed. Three procedures were followed to determine the uncertainty: a combined analytical and numerical analysis of how uncertainties in the pressure measurements propagate through the algorithm, uncertainty evaluation of the LLS surface fitting procedure and evaluation of the uncertainty of the algorithm using data verification test files. The results from the surface fit analysis showed that the contributing errors due to just the local least-squares surface fit are negligible. These uncertainties were on the order of  $10^{-5}$  degrees for angle calculations and  $10^{-3}$  percent for velocity magnitude calculations. Both the analysis of the error propagation through the



algorithm and the uncertainty evaluation with test verification files gave similar results. Angles can be predicted to within 0.6 degrees with 99 % confidence and velocity magnitudes can be predicted to within 1.0 % also with 99 % confidence, while the corresponding uncertainties (standard deviation of the error distribution) are less than 0.2 degrees in angle prediction and less than 0.35% in velocity magnitude prediction.

Appendices D and E provides operation manuals for the two probe calibration algorithms, the neural-network-based algorithm, PROBENET, and the Local-Least Squares (LLS) algorithm, respectively.

## **REFERENCES**

1. Rediniotis, O.K., "The Transient Development of Vortices Over a Delta Wing," Doctoral Dissertation, Virginia Polytechnic Institute and State University, October 1992.
2. Whitmore S.A. and Leondes C.T., "Pneumatic Distortion Compensation for Aircraft Surface Pressure Sensing Devices," *Journal of Aircraft*. Vol. 28, No.12 Dec 1991, pp. 828 – 836
3. Schreck, S. J., Faller, W. E., and Luttgies, M. W., "Neural Network Prediction of Three-Dimensional Unsteady Separated Flow Fields," AIAA Paper No. 93-3426-CP, Monterey, CA, August 1993.
4. Schreck, S. J. and Faller, "Encoding of Three-Dimensional Unsteady Separated Flow Field Dynamics in Neural Network Architectures," AIAA Paper No. 95-0103, Reno, Nevada, January 1995.
5. Fan, X., Herbert T. and Haritonidis, J. H., "Transition Control with Neural Networks," AIAA Paper No. 95-0674, Reno, Nevada, January 1995.
6. Kinser, R.E. and Rediniotis, O.K., "Development of A Nearly-Omni-Directional, Three Component Velocity Measurement Pressure Probe," AIAA Paper No. 96-0037, 34<sup>th</sup> AIAA Aerospace Sciences Meeting, Reno, Nevada, January 1996.
7. Zilliac, G. G., "Calibration of Seven-Hole Probes for Use in Fluid Flows with Large Angularity," NASA TM 102200, December 1989.
8. Larson, T. J., Whitmore, S. A., Ehemberger, L. J., Johnson, J. B. and Siemers, P. M., "Qualitative Evaluation of a Flush Aft data System at Transonic Speeds and High Angles of Attack," NASA TP-271 6, 1987.
9. Larson, T. J., Moes, T. R. and Siemers, P. M., "Wind Tunnel Investigation of a Flush Airdata System at Mach Numbers From 0.7 to 1.4," NASA TM-101697, 1990.
10. Whitmore, S. A, Davis, R. J. and Fife, J. M., "In-Flight Demonstration of a Real-Time Flush Airdata Sensing System," *AIAA Journal of Aircraft*, Vol. 33, Number 5, pp. 970-977, September-October 1996.
11. Whitmore, S. A., Cobleigh, B. R. and Haering, E. A., "Design and Calibration of the X-33 Flush Airdata Sensing System," NASA TM 1998-206540, January 1998.
12. Rohloff, T., J., "Development and Evaluation of Neural Network Flush Airdata Sensing Systems," Ph.D. Dissertation, University of California Los Angeles, Department of Mechanical Engineering, May 1998.



# APPENDIX A



# **Miniature Multihole Pressure Probes and Their Neural-Network-Based Calibration**

O. K. Rediniotis and R. Vijayagopal

Reprinted from

## **AIAA Journal**

Volume 37, Number 6, Pages 666–674



*A publication of the*  
American Institute of Aeronautics and Astronautics, Inc.  
1801 Alexander Bell Drive, Suite 500  
Reston, VA 20191-4344

# Miniature Multihole Pressure Probes and Their Neural-Network-Based Calibration

Othon K. Rediniotis\* and Rajesh Vijayagopal†  
Texas A&M University, College Station, Texas 77843-3141

We present the development of miniature multihole pressure probes and a novel neural-network-based calibration algorithm for them. Seven-hole probes of tip diameters as low as 0.035 in. (0.9 mm) were successfully fabricated with high tip surface quality. Any of the typical probe tip geometries, i.e., hemispherical, conical, or faceted, could be fabricated. The miniature probes were calibrated and tested in a wind tunnel. A backpropagation-based neural-network calibration algorithm was developed for these probes, with flexibility in network architecture design and network self-optimization capabilities. In the feedforward mode the algorithm yields computational speeds an order of magnitude higher than those typically achieved by similar accuracy interpolation algorithms. The new algorithm has prediction accuracies of 0.28 deg in the flow angles and 0.35% in the velocity magnitude.

## Nomenclature

$A_s$	= static pressure coefficient
$A_t$	= total pressure coefficient
$B_c$	= cone-angle pressure coefficient
$B_p$	= pitch-angle pressure coefficient
$B_r$	= roll-angle pressure coefficient
$B_y$	= yaw-angle pressure coefficient
$C_p$	= generic pressure coefficient; could stand for any of $B_p, B_c, B_y, B_r, A_t, A_s$
$E$	= error vector
$\hat{e}$	= sum-squared error
$f_i^h$	= activation function for node $i$ on layer $h$
$I$	= identity matrix
$J$	= error Jacobian matrix
$o_i^h$	= output of node $i$ on layer $h$
$p_i$	= pressure reading at orifice $i$ of the probe
$p^+$	= pressure reading at peripheral port adjacent to port $i$ , in the clockwise direction when looking into the probe tip
$p^-$	= pressure reading at peripheral port adjacent to port $i$ , in the counterclockwise direction when looking into the probe tip
$q$	= characteristic of dynamic pressure
$w_{ij}^h$	= weight applied to the connection to node $i$ on layer $h$ from node $j$ on layer $h - 1$
$x_i^h$	= sum of node weighted inputs
$\alpha$	= pitch flow angle; momentum coefficient
$\beta$	= yaw flow angle
$\delta_i^h$	= error sensitivity per node
$\delta C_p$	= uncertainty in the calculation of $C_p$
$\delta p_i$	= uncertainty in the measurement of pressure $p_i$
$\eta$	= learning rate coefficient
$\theta$	= cone flow angle
$\phi$	= roll flow angle

## I. Introduction

OVER the years multihole probes, such as five- and seven-hole probes, have established themselves as some of the easiest-to-use and cost-effective devices for three-component velocity measurements in research as well as industry environments. They provide accurate flow measurements for flow angles up to 75 deg and

are inexpensive and robust. Furthermore, to minimize flow disturbance, probes of small diameter can be fabricated. Because of their small size, irregularities in manufacturing are unavoidable, which requires that each probe be calibrated individually. Unless the probe tip is physically damaged, it will maintain its structural characteristics, and therefore only one initial calibration is required for the lifetime of the probe.

Because multihole pressure probes are intrusive flow-diagnostics instruments, concerns of probe interference with the flows they are trying to measure always arise. For example, in the case of leading-edge vortical flows over delta wings, the presence of the probe in the neighborhood of the vortex core can induce premature vortex breakdown.<sup>1</sup> Therefore, a strong incentive exists to reduce the probe size, thus reducing the interference. Concurrently, probe-size reduction offers higher spatial resolution for measurements in high-shear flows. Also, when measuring near a surface, a distance of at least four probe diameters should be maintained to avoid wall effects.<sup>2</sup> Smaller probes can measure closer to the surface without violating this proximity rule. However, probe-size reduction presents fabrication as well as frequency response challenges. In terms of fabrication, probe tip-surface quality is important in measurement accuracy. For two different calibration surfaces the smoother surface typically yields higher prediction accuracies. This is self-evident if one considers the fact that typical interpolation techniques use smooth continuous functions to locally model the calibration surface. The smoothness of the calibration surface depends, in turn, on the tip-surface quality. Maintaining the same relative tip-surface roughness (average tip-surface imperfection size divided by the probe diameter) becomes a fabrication challenge as the probe diameter decreases. For the present work we were able to reduce the probe diameter to as low as 0.035 in. (0.9 mm), maintaining the same high surface quality of typical 0.125-in. (3.17-mm)-diam probes. In a different challenge, as the probe diameter decreases, the tubing frequency response decreases. Because this is beyond the scope of the present work, for a treatment of this problem the reader is referred to Vijayagopal et al.<sup>3</sup>

Probe calibration is generally performed by placing the probe in a flowfield with known velocity magnitude and direction. The probe is pitched and yawed (or coned and rolled) through a range of angles to cover the range of possible velocity vector orientations. For each probe orientation the pressures from the five (or seven) pressure ports are recorded. This procedure is typically performed for angle increments of 2–5 deg, resulting in approximately 1000–3000 discrete calibration points, for a cone-angle range of 0–75 deg and the entire roll-angle range (0–360 deg).

After the probe has been calibrated, it can be used to measure the flow properties in an unknown flowfield. By measuring the probe port pressures at a point and comparing them to the calibration data, estimates of the flow angles and the velocity magnitude can be made. This comparison process is achieved by the calibration algorithm.

Presented as Paper 98-0204 at the AIAA 36th Aerospace Sciences Meeting, Reno, NV, Jan. 12–15, 1998; received April 8, 1998; revision received Feb. 12, 1999; accepted for publication Feb. 19, 1999. Copyright © 1999 by the American Institute of Aeronautics and Astronautics, Inc. All rights reserved.

\*Assistant Professor, Department of Aerospace Engineering, Member AIAA.

†Graduate Research Assistant, Department of Aerospace Engineering.

In the present work a neural-network-based calibration algorithm was successfully developed. Before we present it, a brief overview of different types of calibration algorithms used in the past is given next.

For hemispherical probe tips one calibration method used the potential flow solution for flow over a sphere to relate flow angle and velocity to pressure differentials measured by the probe.<sup>4</sup> The technique was demonstrated by calibrating a hemispherical-tip five-hole probe. This method can be sensitive to construction defects of the probe tip and is generally accurate to only a few degrees at best. Interpolation techniques are widely used with multihole probe calibration data. Zilliac,<sup>5</sup> in his calibration of conical seven-hole probes for use in flows with large angularity, used the Akima (IMSL subroutine) interpolation procedure. For each calibration point the seven probe pressures and the total pressure are recorded along with the calculated pressure coefficients and the known roll and cone (or pitch and yaw) angles. Then, when test data are collected, the relevant coefficients are calculated and compared to the stored calibration database. By locating calibration points with pressure coefficient values similar to the measured coefficients, the approximate flow conditions are identified. The adjacent coefficient values are then interpolated to yield the precise flow properties. The technique yields good accuracy. However, the present authors' experience with the Akima interpolation procedure is that it is time consuming. This procedure is not suitable especially for applications, like air-data systems for example, where tens of readings per second are necessary.

Alternatively, empirical relationships can be derived in terms of the pressure coefficients over the different flow regions of the probe.<sup>6</sup> In Ref. 6 the measurement regions of a five-hole probe were divided into the low-angle regime and four high-angle regimes corresponding to the center hole and each one of the four peripheral holes, respectively. The calibration data were used to derive empirical relationships representing the pitch and yaw angles of the velocity vector in terms of the measured pressure coefficients for five-hole hemispherical probes. Using a fixed number of points, polynomial curve fits were made through the known calibration points to describe the variation of the flow variables over the measurement domain. Rediniotis et al.<sup>7</sup> derived bicubic polynomial fits through the calibration data for a conical seven-hole probe. Further, they increased the number of regions for which polynomials were identified. This resulted in eight low-angle regions and 32 high-angle regions, thus improving the description of the probe measurement domain. This technique guarantees agreement with the calibration points but does not necessarily ensure well-behaved calibration surfaces between calibration points.

Artificial neural networks have been effectively applied to mechanical and control systems. In aerodynamics, neural networks have proven their worthiness both as installed components in the aircraft control systems as well as research tools to investigate, model, and control fluid flows.<sup>8-10</sup> Neural networks were coupled with flow measurement tools such as an omnidirectional pressure probe to investigate separated and recirculating flows.<sup>11</sup> In the present work a novel neural-network calibration scheme has been formulated for use in the calibration of multihole pressure probes (five-hole or seven-hole). This procedure uses a large database of calibration information taken over a large range of flow cone angles (up to 75 deg). The calibration data is then used to train a multilayer neural network to predict the flow variables based on calculated pressure coefficients. During the training process, a network information file is generated that contains the necessary details of the network weights and biases. Subsequently, test data presented to the network are processed in a feedforward mode to predict the flow direction and magnitude based on the network's knowledge. This versatile technique allows for nonuniform calibration grids, dense calibration grids, and updating of the calibration data, provides high prediction accuracy, and is very fast in the feedforward mode. Also, the speed in the feedforward mode is independent of the size of the calibration file in contrast to conventional local interpolation algorithms<sup>5,11</sup> of similar accuracy, whose speed is highly dependent on the size of the calibration data file. Moreover, the size of the feedforward code is on the order of a hundred lines, rendering interfacing with existing user codes (such as data-acquisition and data postprocessing codes) extremely easy.

Researchers in the flight-test community have used the principles of multihole probes to develop flush air-data systems.<sup>12-15</sup> In these systems the nose of the aircraft is instrumented with multiple pressure ports, strategically positioned, and in essence operates as a giant multihole probe. In some efforts neural networks have been successfully used, even in real time, to extract air-data information from the pressure measurements,<sup>16</sup> with speeds similar to the algorithm presented here. These air-data systems have a different port arrangement than typical five- and seven-hole probes, a higher number of ports, and are not plagued by calibration issues that emerge as a result of miniaturization. Such an issue, for example, is the transportability of the calibration from one system to another. For the miniature probes discussed here, calibration transportability, without compromising measurement accuracy, is not an option, and each probe has to be calibrated individually. This is because the effect of the probe manufacturing defects on the calibration is inversely proportional to the size of the probe.

## II. Miniature Pressure Probe Fabrication

In what follows the probe diameter range indicated by "miniature" is between 0.035 and 0.065 in. (0.9 and 1.65 mm). The construction of probes can be divided into the fabrication of internal and external features. The external features define the geometry exposed to the flow. The internal features define the discreet pressure channels that transmit the pressure from the probe tip to the pressure transducers.

### External Features

Figure 1 illustrates the arrangement of the probe components. Probe tips are typically made of brass, with the exception of the smallest probe (0.035 in. or 0.9 mm in diameter). There are three parameters defining the tip geometry and features: 1) diameter (0.035–0.065 in. or 0.9–1.65 mm), 2) shape (conical, hemispherical, faceted), and 3) number of holes (5 or 7). The first extension (Fig. 1) precisely matches the outside diameter of the tip and is typically up to 20 diameters long. Ferrules gradually increase the outside diameter of the probe shaft, providing the strength of material necessary for a given length. If needed, a second extension can be added, creating a very long probe for special applications. Mounts are typically hexagonal to allow for probe roll referencing with the flat surfaces aligned with the hole pattern of the tip.

### Internal Features

Each of the holes in the probe tip leads to a stainless-steel tube with its inside diameter matching the diameter of the hole. As the probe shaft diameter increases, each tube is telescoped into a larger tube, which finally protrudes from the back of the mount. Each connection is soldered and tested for strength and leakage. The final assembly is also tested for pressure cross-talk, i.e., pneumatic communication between two or more probe holes and their associated tubing. Pictures of the miniature probes fabricated at the Aerospace Engineering Department of Texas A&M University are shown in Figs. 2a–2g. Figure 2a shows a probe with conical tip, 0.035 in. (0.9 mm) in diameter, whereas Fig. 2b shows a faceted tip, 0.065 in. (1.65 mm) in diameter (in all pictures, the coin is a dime). Figure 2c is an assortment of probes with conical and hemispherical tips, 0.035, 0.065, and 0.125 in. (or 0.9, 1.65, and 3.17 mm) in diameter. Figures 2d–2f show different zoomed-in views of a probe with a conical tip, 0.04 in. (1 mm) in diameter. Figure 2g shows the end view of a hemispherical five-hole probe with tip diameter 0.065 in. (1.65 mm).

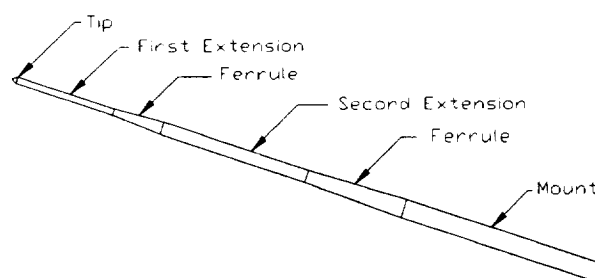


Fig. 1 Schematic of miniature probe assembly.

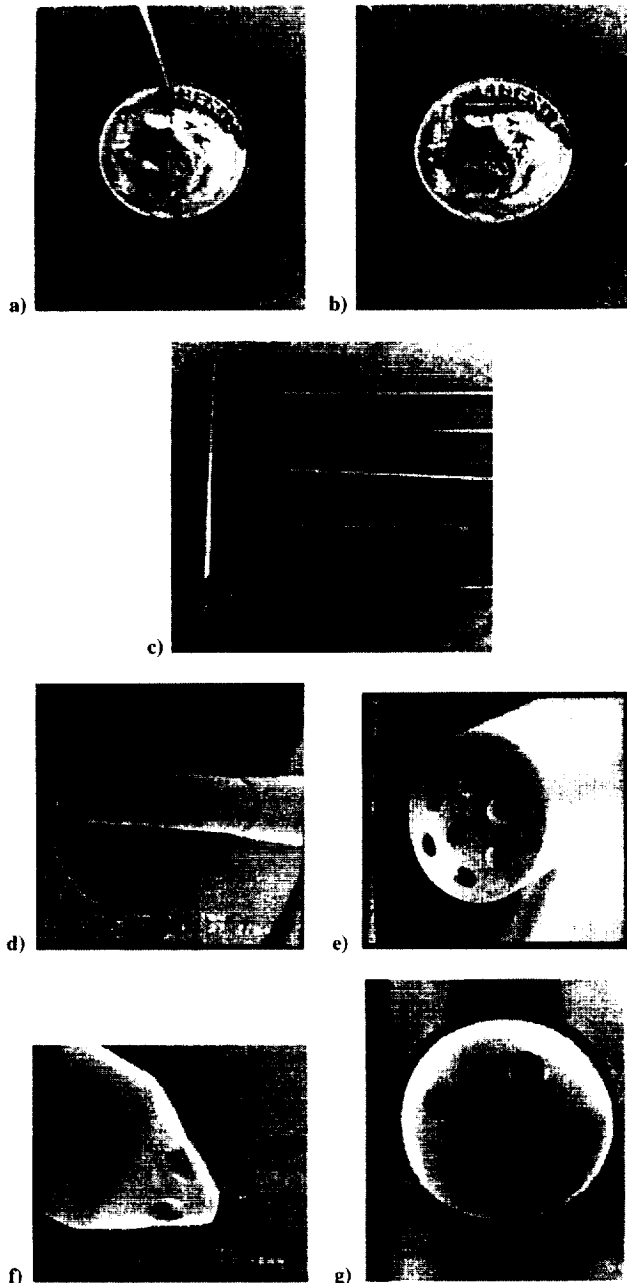
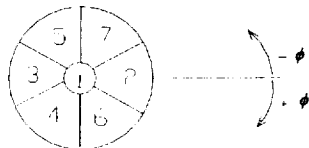


Fig. 2 Miniature probe pictures: a) probe with conical tip, 0.035 in. (0.9 mm) in diameter; b) faceted probe tip, 0.065 in. (1.65 mm) in diameter; c) assortment of probes with various tip geometries; d) electron microscope picture of probe with conical tip, 0.04 in. (1 mm) in diameter; e) and f) closer tip views for the probe of Fig. 2d; and g) electron microscope picture of hemispherical tip, 0.065 in. (1.65 mm) in diameter.

Fig. 3 Seven-hole measurement domain divided into seven sectors, each centered on an individual pressure port numbered 1-7.



### III. Probe Calibration Background

A brief overview of the probe calibration theory is given next for the case of the seven-hole probe. The flow over a seven-hole probe can be typically divided into two regimes: low-angle and high-angle flow. The low-angle flow regime is defined as the velocity inclination range for which the pressure registered by hole #1 (Fig. 3) is the highest among the seven measured pressures. The flow remains attached over the entire probe; therefore, a unique set of seven pressures exists at every probe orientation with respect to the flow. The

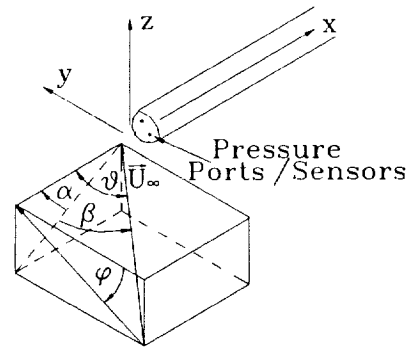


Fig. 4 Flow angle and probe coordinate system definition.

orientation of the probe with respect to the flow is defined by two angles: the pitch-angle  $\alpha$  and the yaw-angle  $\beta$  (Fig. 4). For high-angle flows the  $i$ th hole registers the maximum pressure  $p_i$ , where  $i$  takes a value from 2 through 7. The flow may not be attached over the entire probe. For high-angle flows the position of the probe with respect to the flow is more conveniently defined in spherical coordinates. The two orientation angles are the cone-angle  $\theta$  and the roll-angle  $\phi$  (Fig. 4).

At every measurement location in a flow-mapping experiment, the local velocity vector can be fully characterized by four variables. In the low-angle regime the variables are pitch-angle  $\alpha$ , yaw-angle  $\beta$ , total pressure coefficient  $A_t$ , and the static pressure coefficient  $A_s$ . In the high-angle regime the four variables are cone-angle  $\theta$ , roll-angle  $\phi$ , and the pressure coefficients  $A_t$  and  $A_s$ . Knowledge of the local temperature is also required; however, for the flows of interest here the temperature is constant and equal to the freestream temperature, which is measured and known. The four variables need to be determined as functions of the measured pressures or the two nondimensional pressure coefficients formed from these pressures:  $B_p$ ,  $B_y$  for low-angle flow and  $B_c$ ,  $B_r$  for high-angle flow. The definitions are as given next.

#### Low-Angle Regime (Sector 1)

Independent (Input) Variables:

$$B_p = \frac{1}{\sqrt{3}} \cdot \frac{(p_7 + p_5 - p_4 - p_6)}{q} \quad (1)$$

$$B_y = \frac{(p_2 - p_3)}{q} + \frac{(p_6 - p_5 + p_7 - p_4)}{2 \cdot q}$$

Dependent (Output) Variables:

$$A_t = \frac{(p_1 - p_t)}{q}, \quad A_s = \frac{(p_1 - p_s)}{q} \quad (2)$$

Pitch-angle,  $\alpha$       Yaw-angle,  $\beta$

where  $q = p_1 - [(p_2 + p_3 + p_4 + p_5 + p_6 + p_7)/6]$ ,  $p_t$  is the local total pressure, and  $p_s$  is the local static pressure.

#### High-Angle Regimes (Sectors 2-7)

Independent (Input) Variables:

$$B_c = \frac{(p_i - p_t)}{q}, \quad B_r = \frac{(p^+ - p^-)}{q} \quad (3)$$

Dependent (Output) Variables:

$$A_t = \frac{(p_i - p_t)}{q}, \quad A_s = \frac{(p_i - p_s)}{q} \quad (4)$$

cone-angle,  $\theta$       roll-angle,  $\phi$

where  $q = p_i - [(p^+ + p^-)/2]$  and  $p_i$  is the highest measured pressure (at the  $i$ th port). Looking into the probe tip,  $p^+$  and  $p^-$  are the

pressures measured by the peripheral holes adjacent to port  $i$  in the clockwise and counterclockwise direction, respectively.

#### IV. Artificial Neural-Network Architecture, Training, and Optimization

##### Network Architecture

An artificial neural network is composed of processing elements called nodes, with each node having several input branches but only one output branch. Each input connection to a node has a weight associated with it. The input values are multiplied by the associated weights and summed together with a node bias value. An activation function then acts on the summed value producing the output value for the node. An artificial neural network is built of several layers of nodes with the first layer typically having as many nodes as there are input variables. The number of middle or hidden layers is application dependent. Figure 5 shows a typical network structure, which could be used to train and predict the pitch-angle. All of the node interconnections are shown. The input layer accepts two input elements. There are two hidden layers and one output layer. The output of each node in a layer serves as input to the nodes of the next layer. In Fig. 5,  $f_1$ – $f_9$  are the activation functions applied at each node.

A node's output  $o_i^h$  is given by

$$x_i^h = \sum_j w_{ij}^h o_j^{h-1}, \quad o_i^h = f_i^h(x_i^h) \quad (5)$$

where superscript  $h$  denotes the layer number, subscript  $i$  denotes the node in question, and subscript  $j$  denotes the node in the previous ( $h - 1$ ) layer.

The artificial neural-network algorithm that has been developed uses coefficients calculated from probe calibration pressure data for the training of a set of neural networks. For the seven-hole probe each network uses two system inputs, the two pressure coefficients  $B_p$  (or  $B_r$ ),  $B_y$  (or  $B_r$ ), and four system outputs,  $A_r$ ,  $A_x$ , pitch  $\alpha$  (or cone  $\theta$ ), and yaw  $\beta$  (or roll  $\phi$ ) angles. A large training set of data containing cone and roll angles and the pressure information is taken using a calibration apparatus.<sup>11</sup> The pressures are reduced to the relevant pressure coefficients. The network uses this information as its training data and, through a training algorithm, adjusts its weights to minimize the resultant error between the predicted and the exact values of the outputs. Once the network is trained, measured pressure data that may or may not coincide with the training data can be input to the network, which then predicts the flow variables (velocity and angles) corresponding to the measured pressures.

If the high-angle sectors were further split up to improve the description of the measurement domain as shown in Fig. 6, higher prediction accuracy could be achieved. This was expected from our previous neural-network experience in which it became repeatedly obvious that, the more complicated the function to be represented and the bigger its definition domain, the harder the task of finding a neural network with high modeling accuracy. So the high-angle

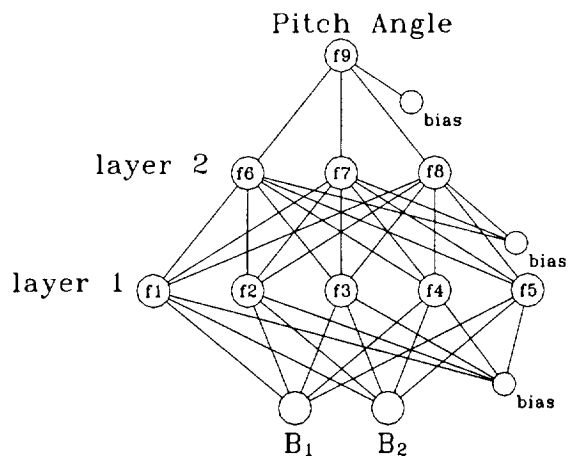


Fig. 5 Typical network structure that takes a two-element input to train for and predict the pitch-angle.

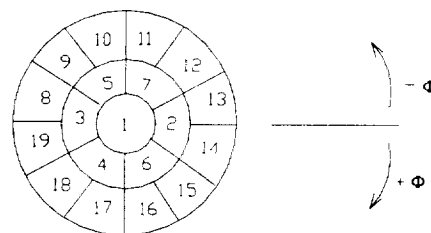


Fig. 6 Seven-hole domain split up to enhance neural-network performance.

sectors were first split into low-high and high-high regimes. The high-high regimes were further split laterally (in roll). For example, sector 2 of Fig. 3 was replaced by three such subsectors in Fig. 6: 2 (low-high), and 13, 14 (high-high). In this way a seven-hole probe was split up to have as many as 19 sectors. Care was taken to ensure that there was at least a 5-deg overlap (in cone and roll) between adjacent sectors. This is done to deal with calibration and test points that lie near the borders of adjacent sectors.

##### Artificial Learning

An artificial neural network learns by adjusting the values of its weights through a training process. The training process consists of giving the neural-network sample input-output data pairs and letting the neural-network algorithm adjust the weights until it can produce the correct output for each input. This procedure is called *supervised learning*. Backpropagation is one method of self-correction. During this process, input is applied to the first layer of a neural network and propagated through until an output is generated at the last layer of the neural network. The output obtained through forward propagation is then compared with the desired output to generate an error signal. The error is then distributed back to the nodes of the previous layer according to their contribution to the error. This process is repeated for all layers, updating the weights. The neural network is iteratively trained with several input-output vector sets until it has all of the training data encoded into it. Once the network has correctly encoded the training data, it can process input data according to the parameters set forth by the training process. It is important to note that the trained neural network will perform only as well as the training data allows. For this reason, care should be taken in selecting the set of training vectors.

Typically, the question of error convergence to a local or global minimum arises. If the backpropagation algorithm converges to a local minimum, learning will then cease, and the error of the network output may be unacceptably high. Two simple methods of dealing with this circumstance are to increase the number of hidden layers or to start over the training process with a different set of initial weights. When the backpropagation algorithm does reach an acceptable solution, there is no guarantee that it has reached the global minimum. But as long as the solution is acceptable from an error standpoint, convergence to a local minimum is irrelevant. To avoid the situation of the algorithm converging to a local minimum without reaching a desired minimum error, momentum learning was implemented in the code. Momentum learning allows the network to respond, not only to the local gradient of the error surface, but also to recent trends in the error surface. The algorithm is thus less likely to get trapped in local minima. To speed up convergence, adaptive learning was also implemented. Adaptive learning allows the learning rate to vary depending on the output error. This allows the network to adapt the learning rate to the local terrain of the error surface. When a larger rate is possible for stable learning, the rate is increased. When smaller learning rate is required, the rate is automatically decreased.

The training algorithm accepts as its input a raw pressure data file containing the calibration data for the probe. This data file is then converted to training vector files for every sector of the probe. The training vector files are used to train the neural networks by backpropagation. Weight initialization is performed either by generating random weights or by using existing weights files from previously trained similar networks. During training, the weight matrices are updated using a steepest descent technique to progress toward the

minimum error. The error is calculated at each node on the output layer as the difference in the predicted and known outputs:

$$\delta_k^H = \frac{df_k^H(x_k^H)}{dx_k^H} (o_k^H - \text{known}) \quad (6)$$

where  $\delta_k^H$  is the error sensitivity for node  $k$  on the output layer  $H$ . The error is backpropagated through the network by the following recurrence relation<sup>17-20</sup>:

$$\delta_i^{h-1} = \frac{df_i^{h-1}(x_i^{h-1})}{dx_i^{h-1}} \sum_k w_{ki}^h \delta_k^h, \quad h = 2 \dots H \quad (7)$$

For each of the nodes in the hidden layers,  $\delta_i^h$  represents the contribution of error to the network output. The weight changes at each node are then calculated by the following learning rule<sup>18</sup>:

$$\Delta w_{ij}^h(t+1) = \alpha \Delta w_{ij}^h(t) + (1 - \alpha) \eta \delta_i^h o_j^{h-1} \quad (8)$$

where  $\Delta w_{ij}^h(t)$  is the change in weights for layer  $h$  at iteration  $t$ ,  $o_j^{h-1}$  is the output of node  $j$  on layer  $h-1$ , and  $\delta_i^h o_j^{h-1}$  is the estimated error gradient calculated for each weight, which can be expressed as

$$\frac{\partial \hat{e}}{\partial w_{ij}^h} = \delta_i^h o_j^{h-1} \quad (9)$$

As already mentioned, to aid in convergence a momentum term  $\alpha$  is used to dampen the oscillations in the convergence and the adaptive learning rate term,  $\eta$  is used as a type of dynamic and under-relaxation for updating the weight matrices. The learning rate is increased, and the weights are updated after each iteration that reduces the sum-squared error  $\hat{e}$  of the network. After each unsuccessful iteration the learning rate is decreased, and the weight changes are discarded.

To further improve the convergence rate, the Levenberg-Marquardt optimization method was implemented<sup>21</sup>:

$$\Delta W = (J^T J + kI)^{-1} J^T E \quad (10)$$

Here  $J$  is the error Jacobian matrix consisting of the partial derivatives of the error terms with respect to the node weights,  $k$  is a scalar, and  $E$  is the error vector determined from the known vector output and the network calculated values. When  $k$  is large, the expression is approximately the gradient descent method. When  $k$  is small, the expression approximates the Newton method.<sup>20</sup> Because the second method is faster but tends to be less accurate when near an error minimum, the scalar  $k$  is adjusted like the adaptive learning rate. As long as the error decreases,  $k$  is made larger. If the error increases,  $k$  is made smaller. Further, residual monitoring and active perturbation of the weight matrices are additional methods used by the algorithm to ensure satisfactory convergence and to stimulate learning.

#### Network Optimization

Different network architectures will obviously produce different levels of prediction accuracy. Procedures to find the optimum network structure for specific problems have so far been primarily based on trial and error. Ideally, the neural-network code should develop its own intelligence and experience in deciding on the optimum architecture rather than the user being tied to hours of tedious, manual interrogation. In the present code, although the user can at any time override the code's decisions, an expandable heuristic rule base is incorporated that guides the algorithm in the optimal network selection. The main function of these rules is to associate a certain problem or a certain class of problems to certain optimal network architecture or a range of optimal architectures. The main function of the code's optimizer is to generate and train different network architectures and, by comparing their relative performance for a specific problem, conclude on a set of optimal architectures. It can generate optimal network architectures for five-hole probes, seven-hole probes, conical, hemispherical, and faceted tip geometries and spherical omni-probes. For the probes calibrated here the typical optimal architecture consisted of one input layer, two hidden layers, and one output layer; and the number of nodes per hidden layer were typically eight and four for the first and second hidden layer,

respectively. The activation functions that worked the best were linear, sine, cosine, hyperbolic tangent, and sigmoid.

#### V. Calibration Hardware and Setup

Pressure data acquisition during probe calibration and use was performed with a 32-transducer electronic pressure scanner (ESP) from PSI, Inc., with a pressure range of  $\pm 10$  in H<sub>2</sub>O. The ESP was interfaced to a laboratory computer and was calibrated on-line. The calibration was performed using the apparatus described in Kinser and Rediniotis.<sup>11</sup> A 16-bit A/D board from ComputerBoards was used to perform data acquisition. A dual-axis stepper-motor assembly, which is computer controlled, can vary the cone and roll angles ( $\theta$ ,  $\phi$ ) in the ranges (0, 180 deg) and (-180, 180 deg), respectively. The positioning resolution for the calibration assembly is 0.32 deg in cone and 0.9 deg in roll. To be able to assess the accuracy of the calibration technique, test data were also collected, which involved positioning of the probe at several known orientations, ( $\alpha_{\text{test}}$ ,  $\beta_{\text{test}}$ ) or ( $\theta_{\text{test}}$ ,  $\phi_{\text{test}}$ ), none of them coincident with any of the orientations used for calibration, ( $\alpha_{\text{cal}}$ ,  $\beta_{\text{cal}}$ ) or ( $\theta_{\text{cal}}$ ,  $\phi_{\text{cal}}$ ), and collection of the pressures. These pressures were fed into the calibration routines, and a predicted pair ( $\alpha_{\text{pred}}$ ,  $\beta_{\text{pred}}$ ) or ( $\theta_{\text{pred}}$ ,  $\phi_{\text{pred}}$ ) was calculated. The difference between the two pairs ( $\alpha_{\text{test}}$ ,  $\beta_{\text{test}}$ ) and ( $\alpha_{\text{pred}}$ ,  $\beta_{\text{pred}}$ ) or ( $\theta_{\text{test}}$ ,  $\phi_{\text{test}}$ ) and ( $\theta_{\text{pred}}$ ,  $\phi_{\text{pred}}$ ) is a measure of the calibration accuracy, although some bias errors are not included (for example, because of tunnel flow angularity, as seen later in Sec. VI).

Calibration and data acquisition were performed in the Texas A&M 3 × 4 ft Aerospace Engineering Wind Tunnel. This is a closed circuit tunnel with a test section equipped with a breather so that the static freestream pressure is equal to the control room pressure. The clear Plexiglas<sup>®</sup> test section is 4 ft (1.22 m) wide, 3 ft (0.91 m) tall, and 6 ft (1.83 m) long. The contraction ratio is 9:1. The maximum speed achieved in the tunnel is about 150 ft/s (45.7 m/s) with freestream turbulence less than 0.16%. To avoid temperature fluctuations over time, there is an active cooling system to keep the freestream temperature at 60°F (15.6°C) during testing.

#### VI. Discussion of Results and Error Analysis

One of the salient features of the calibration algorithm developed is the range of available control over the network architecture. Typical commercial codes allow for an input layer; a few hidden layers (limited number), each one with a specific activation function for the entire layer; and an output layer with its activation function. The code developed here allows the user to specify different activation functions at each node. The activation functions  $f_1$ – $f_9$  in Fig. 5 can be selected from a database of functions or can be user-defined. These functions include constant, linear, quadratic, cubic, logsig, tansig,<sup>17</sup> cosine, sine, and exponential functions. These functions can be customized and the user can define new activation functions.

To assess the effect of using multiple activation function within a layer, two types of network architectures were trained on data from analytical polynomials and actual probe calibration data. The first architecture had one type of activation function per layer, whereas the second employed multiple functions within a layer. Both network architectures were optimized through the algorithm's optimizer. In the first network architecture the network with the best performance was found to have the following structure: four layers, three of which are hidden, each with a single activation function, linear, quadratic, and cubic, respectively. The optimal network of the second type was a simpler two-layer network. Its single hidden layer used three different node types: linear, quadratic, and cubic. Both architectures have the ability to model a cubic polynomial selected for this test. However, the multifunction network requires only 2 layers, 4 nodes, and 10 weights to achieve better results than the 4-layer, 10-node, 34-weight single-function/layer network. The convergence rate for the multifunction network is markedly better as Fig. 7 illustrates. Of the two architectures, multifunction layer networks have been consistently found to have higher convergence rates and converge to lower error levels.

Once the network has been trained to a satisfactory level of convergence, an output binary file is then created, which contains all of the trained network information. This binary file is used by the feed-forward procedure for reducing any new pressure data acquired with the calibrated probe to the velocity components and the orientation

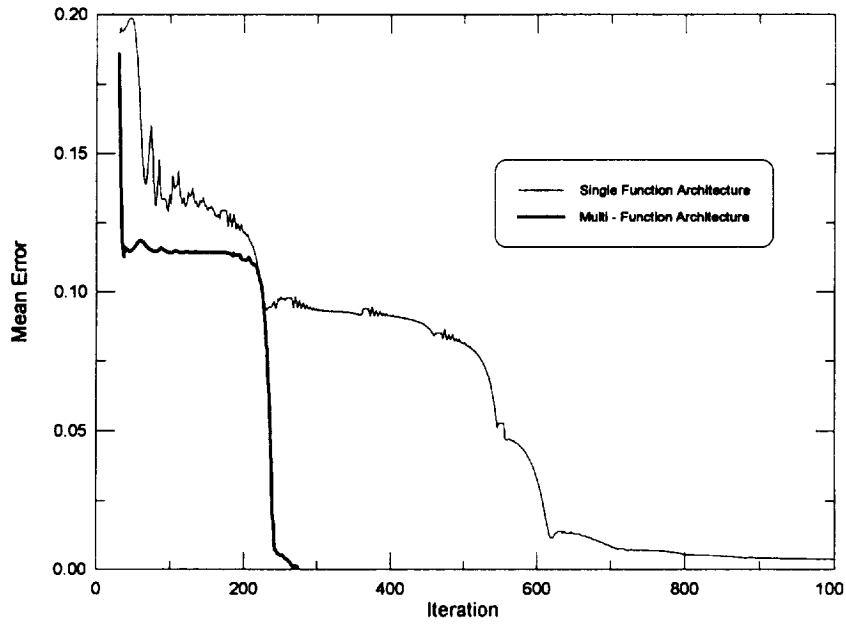


Fig. 7 Convergence history for single and multiple activation function architectures.

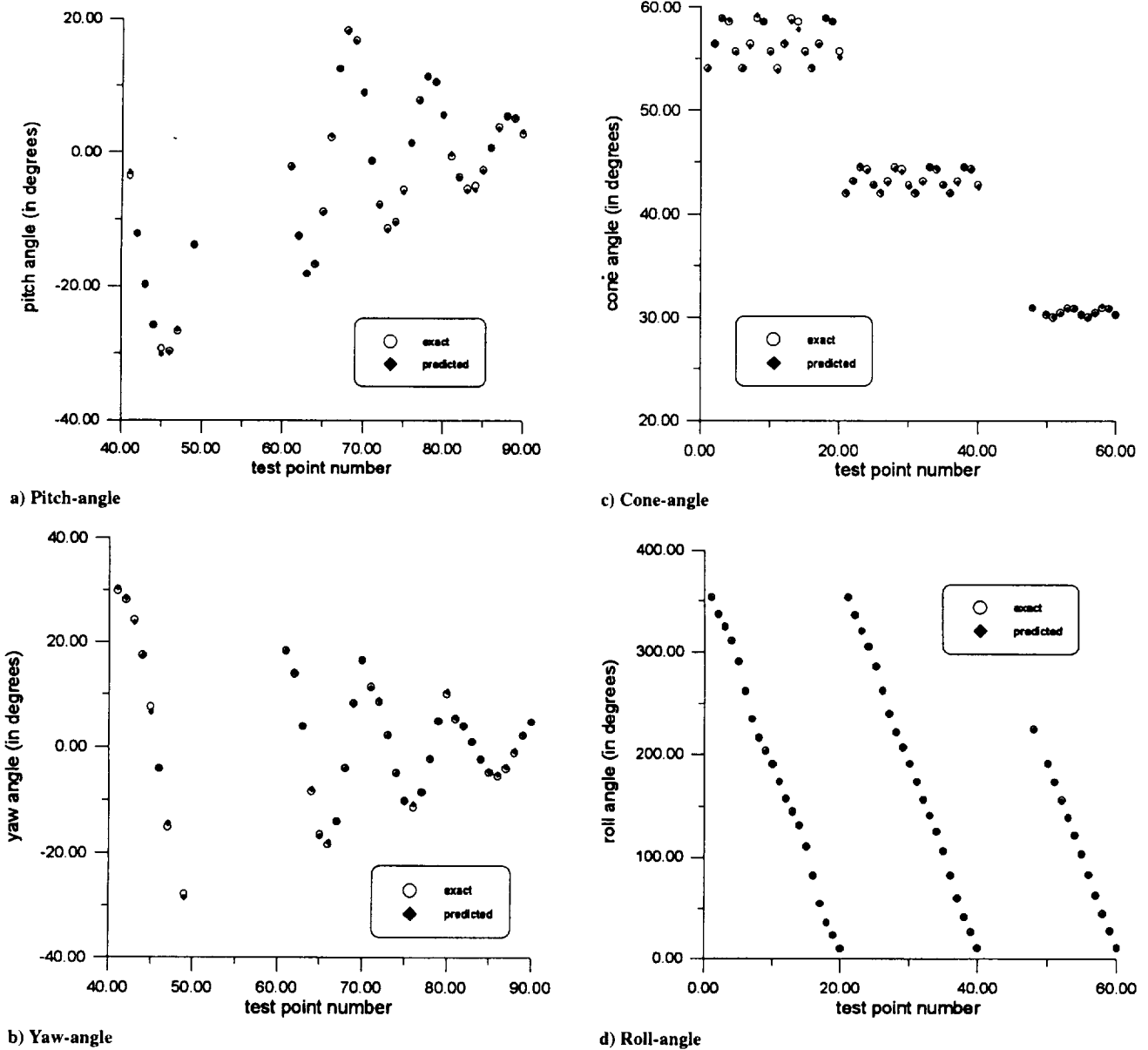


Fig. 8 Neural-network prediction results.

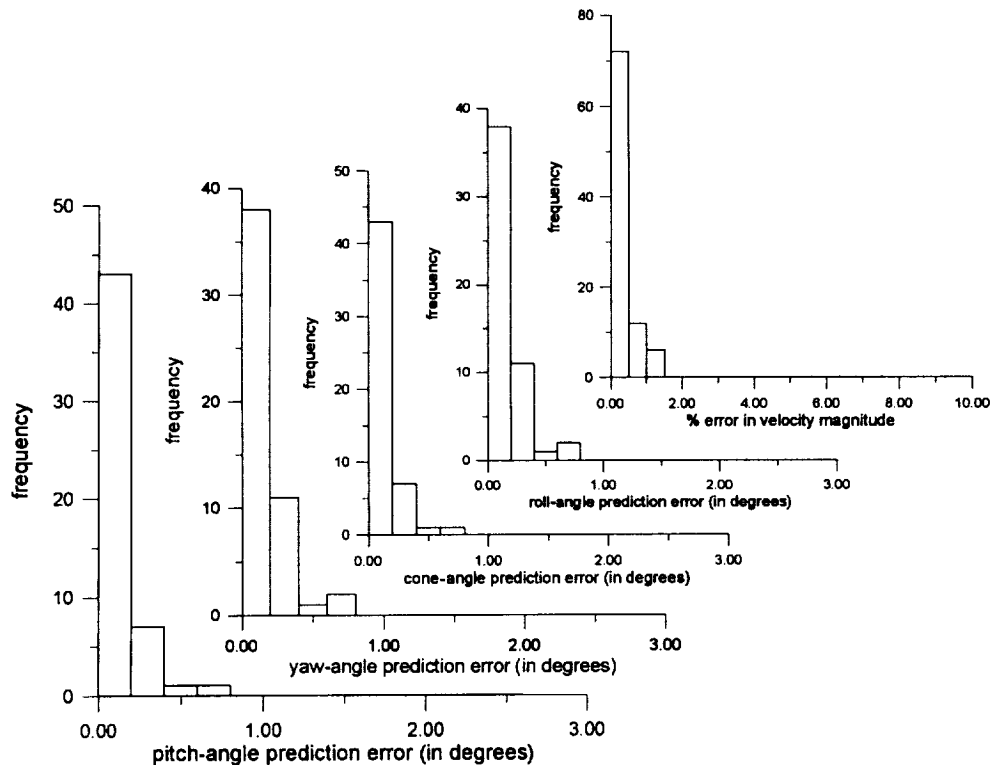


Fig. 9 Prediction error histograms for pitch, yaw, cone, and roll-angle and velocity magnitude.

angles. This feedforward mode is exceptionally fast as compared to similar accuracy local least-squares interpolation techniques<sup>11</sup> and is not dependent on the size of the calibration data file. Typically, the neural-network code can reduce a test data file that contains 100 test points in just about 5 s, whereas the same test file may take about a minute to be processed by the local least-squares interpolation technique. As mentioned in the Introduction, this increased data reduction rate of the neural-network algorithm makes it suitable for applications like air-data systems, where several readings per second are required.

A miniature conical seven-hole probe, 0.063 in. (1.6 mm) in diameter was calibrated at a freestream velocity of 70 ft/s (21.3 m/s). The high-angle sectors were split up as already described to enhance the performance of the networks. Figures 8a–8d show the predictions for the flow angles both in low-angle and high-angle sectors. Typical calibration performance results are shown in Fig. 9 in the form of error histograms. The error is represented along the horizontal axis, while the vertical axis (labeled *frequency*) represents the number of points in a specific error bin. The error band of a specific bin is indicated by the width of the corresponding vertical bar. From these histograms the following error statistics can be calculated: pitch-angle—average absolute error = 0.22 deg, standard deviation of error = 0.26 deg; yaw-angle—average absolute error = 0.28 deg, standard deviation of error = 0.34 deg; cone-angle—average absolute error = 0.15 deg, standard deviation of error = 0.18 deg; roll-angle—average absolute error = 0.17 deg, standard deviation of error = 0.21 deg; and velocity magnitude—average absolute error = 0.35%, standard deviation of error = 0.52%. The higher error levels in the pitch- and yaw-angle prediction (low-angle sector), as compared to the error levels in the cone- and roll-angle prediction (high-angle sectors), are due to the fact that each of the high-angle sectors was further split up to several subsectors, and each subsector was calibrated individually, while no such subdivision was applied to the low-angle sector.

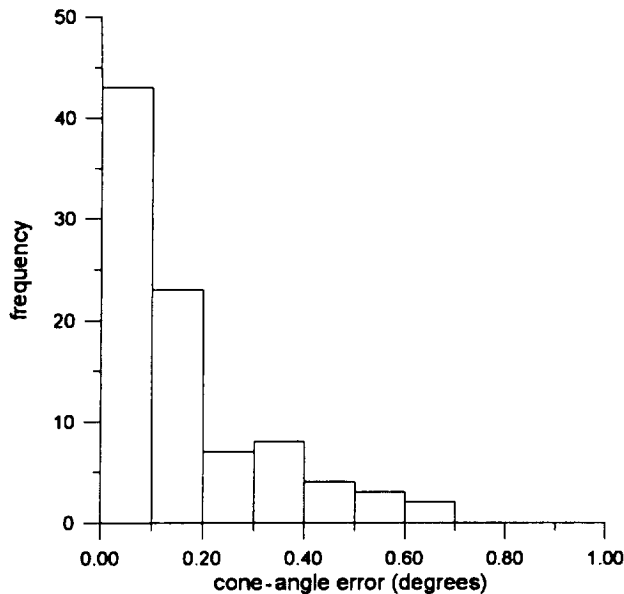
The uncertainty analysis presented next is based on the techniques discussed in Ref. 22, and the application of the techniques to the multihole probe problem follows the procedures discussed in Ref. 23. First, the uncertainty of the pressure measurement hardware is estimated. The pressure scanner used was calibrated during calibration of the probe, on-line, every hour. A 5-point calibration was

performed, which accounted for transducer nonlinearities. The reference manometer used for calibration had an uncertainty of 0.005 torr for the range of pressures used here ( $\pm 6$  torr). The preceding combination, along with a one-count A/D conversion uncertainty of the 16-bit A/D board, yielded a pressure measurement worst-case error of 0.015 torr or 0.009 in  $H_2O$ . Errors in angular positioning were negligible. The resolution of the cone- and roll-positioning stepper motors (0.32 and 0.9 deg) should not be confused with their positioning precision, which is on the order of arc seconds. Slipping of the stepper motors could of course compromise the accuracy, especially because no angular positioning encoders were employed. However, strong evidence (although not absolute proof) that no slipping occurred was the fact that at the end of a calibration session the stepper motors returned the probe, as instructed, to the exact orientation that it started from at the beginning of the session. If any slipping had occurred, it should have happened in a fashion such that all slipping occurrences canceled themselves out, which is a very unlikely event. Bias errors because of probe sting deflection were also negligible at the speeds of calibration and for the specific structural design of the sting. Uncertainty in the tunnel flow angularity will cause a bias error if the probe is tested or used in a different facility. However, for the calibration test processes followed in this work, as described in Sec. V, flow angularity does not have an effect for the following reason. Both calibration and test data were taken in the same facility and freestream velocity, and the calibration apparatus was designed such that it maintained the probe tip always at the same location, regardless of probe orientation.

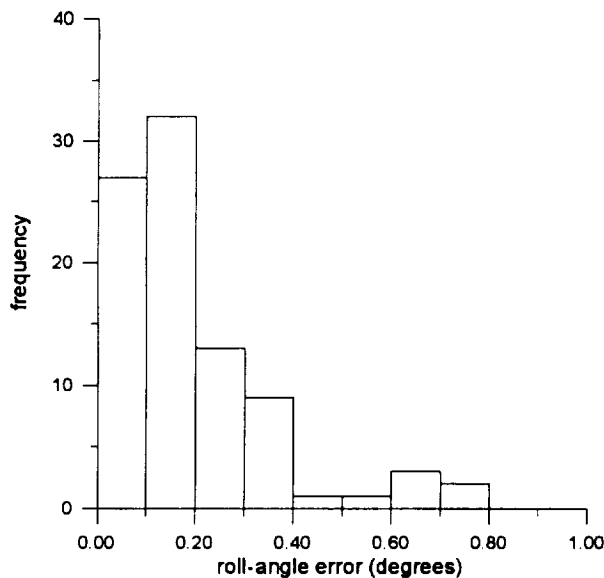
The uncertainty in the evaluation of the pressure coefficients  $B_p$ ,  $B_y$ ,  $B_c$ ,  $B_r$ ,  $A_r$ ,  $A_s$  was calculated using their definition formulas (1)–(4) and constant-odds combination<sup>22</sup> given by

$$\delta C_p = \sqrt{\sum_i \left( \frac{\partial C_p}{\partial p_i} \delta p_i \right)^2} \quad (11)$$

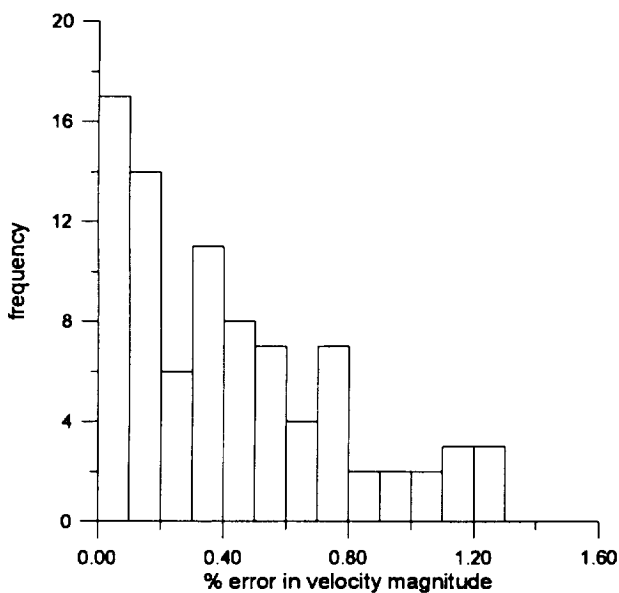
where  $C_p$  is any of the pressure coefficients and  $\delta p_i$  is the uncertainty in the measurement of pressure  $p_i$ . Subsequently, and to see how the uncertainty in the calculation of the pressure coefficients propagates through the neural-network technique, a jitter approach<sup>22</sup> was followed. The estimates of the  $\delta p_i$  were obtained from a Gaussian



a) Cone-angle error



b) Roll-angle error



c) Velocity-magnitude error

Fig. 10 Error histograms derived from uncertainty analysis.

distribution with zero mean and a standard deviation of 0.005 torr. This was chosen so that the worst-case error in pressure measurement, i.e., 0.015 torr, corresponds to three standard deviations from the mean, which in turn corresponds to a 99.5% probability that the pressure measurement error is smaller or equal to 0.015 torr. The preceding allowed the estimation of uncertainty in  $B_p$  (or  $B_c$ ),  $B_y$  (or  $B_r$ ),  $A_l$ , and  $A_r$  for every calibration and test point through Eq. (11). The obtained  $\delta B_p$  (or  $\delta B_c$ ),  $\delta B_y$  (or  $\delta B_r$ ),  $\delta A_l$ , and  $\delta A_r$  were used to perturb the original values of these coefficients for the calibration points, and the perturbed values were subsequently used as the inputs to train the neural networks. Once the networks were trained, they were used to reduce the test data that were also perturbed in the manner just explained. The predictions obtained in this process were compared to those obtained from the unperturbed networks and test points, and the standard deviation of the differences between these two yielded estimates for the overall uncertainty. The results are listed here: standard deviation in cone-angle errors, 0.24 deg; standard deviation in roll-angle errors, 0.37 deg; and standard deviation in velocity magnitude error, 0.72%.

Figure 10 shows the histograms of these errors. The statistical properties of these histograms are very similar to the ones obtained from the actual calibration tests (Fig. 9). As already seen, the error levels obtained from the actual test are within those predicted from the uncertainty analysis. The uncertainty analysis presented here applies strictly to steady-state flows. The issues of probe calibration and measurement accuracy in unsteady flow environments are addressed elsewhere.<sup>3,24</sup>

## VII. Conclusion

Miniature multihole probes were successfully designed and fabricated with high tip-surface quality. Five- and seven-hole miniature probes were fabricated with hemispherical, conical, and faceted tip geometries and tip diameters as low as 0.035 in. A neural-network-based probe calibration algorithm was developed. The algorithm's features include flexibility in network architecture design and network self-optimization capabilities. The introduction of multiple activation function architectures had a significantly positive impact on the network training convergence rates and levels. In the feedforward mode the algorithm yields computational speeds an order of magnitude higher than those typically achieved by similar accuracy interpolation algorithms. Moreover, the small size of the feedforward code facilitates its formulation into a subroutine and enhances its ease of interfacing with other software. A miniature seven-hole probe was calibrated and tested in the wind tunnel. The new algorithm combined with precision probe calibration hardware and procedures yielded prediction accuracies of 0.28 deg in the angle prediction and 0.35% in the velocity magnitude prediction. Finally, an error analysis was performed on the calibration procedures and algorithm and yielded uncertainty levels compatible with those produced by the actual probe test.

## Acknowledgments

This work was supported by NASA Langley Research Center, Flow Modeling and Control Branch, with William Sellers as Monitor, under Grant NAG-1-1753, and by Aeroprobe Corporation under Project 32525-52050. The authors would like to gratefully acknowledge the contribution of Richard Allen, whose machining dexterity made the fabrication of the miniature probes possible.

## References

- <sup>1</sup>Rediniotis, O. K., "The Transient Development of Vortices over a Delta Wing," Ph.D. Dissertation, Dept. of Engineering Science and Mechanics, Virginia Polytechnic Inst. and State Univ., Blacksburg, VA, Oct. 1992.
- <sup>2</sup>Hoang, N. T., "The Hemisphere-Cylinder at an Angle of Attack," Ph.D. Dissertation, Dept. of Engineering Science and Mechanics, Virginia Polytechnic Inst. and State Univ., Blacksburg, VA, Dec. 1991.
- <sup>3</sup>Vijayagopal, R., Pathak, M. M., and Rediniotis, O. K., "Miniature Multi-Hole Pressure Probes—Their Neural Network Calibration and Frequency Response Enhancement," AIAA Paper 98-0204, Jan. 1998.
- <sup>4</sup>Kjelgaard, S. O., "Theoretical Derivation and Calibration Technique of a Hemispherical-Tipped, Five-Hole Probe," NASA TM-4047, Sept. 1988.
- <sup>5</sup>Zilliac, G. G., "Calibration of Seven-Hole Probes for Use in Fluid Flows with Large Angularity," NASA TM-102200, Dec. 1989.

- <sup>6</sup>Bryer, D. W., and Pankhurst, R. C., "Pressure-Probe Methods for Determining Wind Speed and Flow Direction," Her Majesty's Stationery Office, London, 1971.
- <sup>7</sup>Rediniotis, O. K., Hoang, N. T., and Telionis, D. P., "The Seven-Hole Probe: Its Calibration and Use," *Forum on Instructional Fluid Dynamics Experiments*, edited by C. Dutton, Vol. 152, American Society of Mechanical Engineers, Washington, DC, 1993, pp. 21–26.
- <sup>8</sup>Schreck, S. J., Faller, W. E., and Luttgies, M. W., "Neural Network Prediction of Three-Dimensional Unsteady Separated Flow Fields," AIAA Paper 93-3426, Aug. 1993.
- <sup>9</sup>Schreck, S. J., and Faller, W. E., "Encoding of Three-Dimensional Unsteady Separated Flow Field Dynamics in Neural Network Architectures," AIAA Paper 95-0103, Jan. 1995.
- <sup>10</sup>Fan, X., Herbert, T., and Haritonidis, J. H., "Transition Control with Neural Networks," AIAA Paper 95-0674, Jan. 1995.
- <sup>11</sup>Kinser, R. E., and Rediniotis, O. K., "Development of a Nearly-Omnidirectional, Three Component Velocity Measurement Pressure Probe," AIAA Paper 96-0037, Jan. 1996.
- <sup>12</sup>Larson, T. J., Whitmore, S. A., Ehernberger, L. J., Johnson, J. B., and Siemers, P. M., "Qualitative Evaluation of a Flush Aft Data System at Transonic Speeds and High Angles of Attack," NASA TP-2716, June 1987.
- <sup>13</sup>Larson, T. J., Moes, T. R., and Siemers, P. M., "Wind Tunnel Investigation of a Flush Airdata System at Mach Numbers From 0.7 to 1.4," NASA TM-101697, Sept. 1990.
- <sup>14</sup>Whitmore, S. A., Davis, R. J., and Fife, J. M., "In-Flight Demonstration of a Real-Time Flush Airdata Sensing System," *Journal of Aircraft*, Vol. 33, No. 5, 1996, pp. 970–977.
- <sup>15</sup>Whitmore, S. A., Cobleigh, B. R., and Haering, E. A., "Design and Calibration of the X-33 Flush Airdata Sensing System," NASA TM-1998-206540, Jan. 1998.
- <sup>16</sup>Rohloff, T. J., "Development and Evaluation of Neural Network Flush Airdata Sensing Systems," Ph.D. Dissertation, Dept. of Mechanical Engineering, Univ. of California, Los Angeles, CA, May 1998.
- <sup>17</sup>Freeman, J. A., and Skapura, D. M., *Neural Networks Algorithms, Applications and Programming Techniques*, Addison-Wesley, Reading, MA, 1992.
- <sup>18</sup>Fausett, L., "Fundamentals of Neural Networks Architectures, Algorithms, and Applications," Prentice-Hall, Englewood Cliffs, NJ, 1994.
- <sup>19</sup>Hagan, M., Demuth, H., and Beale, M., *Neural Network Design*, PWS Publishing, Boston, MA, 1996.
- <sup>20</sup>Hassoun, M. H., *Fundamentals of Artificial Neural Networks*, MIT Press, Cambridge, MA, 1995.
- <sup>21</sup>Demuth, H., and Beale, M., "MATLAB Neural Network Toolbox," The Mathworks, Inc., Natick, MA, 1997.
- <sup>22</sup>Moffat, R. J., "Contributions to the Theory of Single-Sample Uncertainty Analysis," *Transactions of the ASME*, Vol. 104, June 1982, pp. 250–258.
- <sup>23</sup>Zilliack, G. G., "Modeling, Calibration, and Error Analysis of Seven-Hole Pressure Probes," *Experiments in Fluids*, Vol. 14, No. 1/2, 1993, pp. 104–120.
- <sup>24</sup>Rediniotis, O. K., Johansen, E., Tsao, T., Seifert, A., and Pack, L., "MEMS-Based Probes for Velocity and Pressure Measurements in Unsteady and Turbulent Flowfields," AIAA Paper 99-521, Jan. 1999.

J. Seitzman  
Associate Editor





# **APPENDIX B**



# **Simple Technique for Frequency-Response Enhancement of Miniature Pressure Probes**

O. K. Rediniotis and M. M. Pathak

Reprinted from

**AIAA Journal**

Volume 37, Number 7, Pages 897-899



*A publication of the*  
American Institute of Aeronautics and Astronautics, Inc.  
1801 Alexander Bell Drive, Suite 500  
Reston, VA 20191-4344

# Technical Note

TECHNICAL NOTES are short manuscripts describing new developments or important results of a preliminary nature. These Notes cannot exceed 6 manuscript pages and 3 figures; a page of text may be substituted for a figure and vice versa. After informal review by the editors, they may be published within a few months of the date of receipt. Style requirements are the same as for regular contributions (see inside back cover).

## Simple Technique for Frequency-Response Enhancement of Miniature Pressure Probes

Othon K. Rediniotis\* and Mahesh M. Pathak†

Texas A&M University, College Station, Texas 77843-3141

### I. Introduction

THIS Note deals with the implementation of a simple technique to correct for the pressure measurement error produced in miniature multihole pressure probes caused by the lag in the response of the probe tubing system. As the size of the pressure probe is reduced in order to reduce flow disturbance, the probe's frequency response deteriorates. Reduced frequency response generally causes the wait times in flow-mapping experiments to increase. The wait time is the time that the probe, after it moves to a new measurement location in the flowfield, has to wait before data acquisition can be performed, in order for the pressures at the probe pressure transducers to reach steady state. Moreover, deterioration of probe frequency response limits its capability to resolve temporal information in unsteady flows. In the present work, we introduce a simple algorithm that significantly improves a probe's frequency response. Detailed work in the area was carried out by Whitmore.<sup>1</sup> He developed a mathematical model for a tubing system, derived from the Navier-Stokes and continuity equations. On the basis of this model, he then developed an algorithm to compensate for pneumatic distortion. The technique presented here is simpler and much less computationally intensive and is thus amenable to real-time implementation. The technique presented here is applicable only to critically damped or overdamped tubing systems, as discussed later.

Generally, in pressure-measuring systems such as multihole probes, the pressure at the pressure-measuring instrument (pressure transducer) can be different from the pressure at the source (i.e., the probe tip) because of the time lag and pressure attenuation in the transmission of pressures in the associated tubing. When the pressure at the pressure source is changing rapidly, the pressure at the transducer lags behind that at the source and its amplitude is attenuated because of 1) the time needed for the pressure change to propagate along the tubing (acoustic lag) and 2) the pressure drop associated with the flow through the tubing (pressure lag).<sup>2</sup>

The speed of the pressure propagation along the tubing is the speed of sound. The magnitude of the acoustic lag  $\tau$  thus depends on only the speed of sound  $a$  and the length of the tubing  $L$ , as expressed in  $\tau = L/a$ . Because the speed of sound at standard atmospheric conditions is on the order of 1100 ft/s (340 m/s), errors caused by acoustic lag are of concern only in pressure systems having very long pressure tubing. Errors associated with acoustic lag can be neglected here because the tubing lengths of interest are very short [order of 1 ft (0.3 m)]. Moreover, because of the motion of the air through the pressure tubing between the pressure source and the transducer, the

pressure at the transducer is different from the pressure at the source by a pressure drop  $\Delta p$ . The modeling<sup>1-3</sup> of both of these factors and the simplification of the model are briefly discussed next.

### II. Modeling of Pressure-Tubing Response

Let us consider a section of pressure tubing of length  $L$  and inside diameter  $d$ . Let one end of the tubing be connected to a high-frequency-response pressure transducer (transducer T2) and a transient pressure signal  $p(t)$  from the pressure source be applied to the other end (Fig. 1). Let the pressure measured by transducer T2 be  $p'(t)$ . The pressure signal  $p(t)$  from the pressure source is measured directly by a second pressure transducer T1 (Fig. 1). The tubing assembly can be modeled as a second-order dynamic system<sup>2</sup>:

$$p(t) = mC \frac{d^2 p'(t + \tau)}{dt^2} + RC \frac{dp'(t + \tau)}{dt} + p'(t + \tau) \quad (1)$$

In the preceding expression,  $m$  is the equivalent mass of the system. This is the combined mass of the air inside the tubing and the transducer cavity.  $1/C$  is the system elastic constant,  $R$  is the viscous damping coefficient, and  $\tau$  is the acoustic lag. If we assume laminar flow in the tubing, then the value of  $\lambda = RC$  can be calculated theoretically from the following equation<sup>3</sup>:

$$\lambda = \frac{128\mu LV}{\pi d^4 p_0}$$

where  $L$  and  $d$  are the length and internal diameter of the tubing,  $V$  is the combined volume in the tubing and the transducer cavity,  $p_0$  is a reference pressure in the tubing-transducer system, and  $\mu$  is the coefficient of viscosity of the fluid medium in the tubing (air in our case). This equation assumes laminar flow in the tubing and applies only to straight tubing of constant diameter. The preceding expression for  $\lambda$  does not hold for a more complex tubing assembly, consisting of tubing sections of different lengths and diameters and/or incorporating bends.

For complicated tubing assemblies, such as those in a probe, theoretical calculation of  $\lambda$  is not practical. As shown later, experimental calculation of  $\lambda$  can yield good results. For small tubing and transducer cavity volumes, one can see that

$$mC \ll RC, \quad \tau \ll RC \quad (2)$$

Combining Eqs. (1) and (2), we get

$$\lambda \frac{dp'(t)}{dt} + p'(t) = p(t) \quad (3)$$

The preceding equation, because it is first order, holds for any critically damped or overdamped (and not underdamped) tubing assembly regardless of its complex design. The lag constant  $\lambda$  is of course different for different tubing assemblies. If the system lag constant  $\lambda$  is known, the actual pressure signal  $p(t)$  applied to

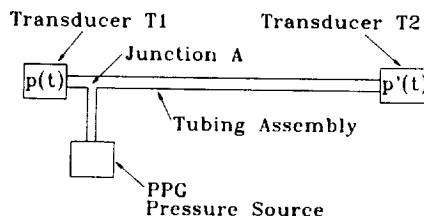


Fig. 1 Schematic of the tubing-transducer assembly.

Received 9 April 1998; revision received 1 March 1999; accepted for publication 4 March 1999. Copyright © 1999 by the American Institute of Aeronautics and Astronautics, Inc. All rights reserved.

\*Assistant Professor, Department of Aerospace Engineering, Member AIAA.

†Graduate Research Assistant, Department of Aerospace Engineering.

one end of the pressure tubing can be calculated from the measured signal  $p'(t)$ , using Eq. (3), even before steady state has been reached.

### III. Experimental Calculation of the Lag Constant $\lambda$

The lag constant  $\lambda$  can be experimentally determined in several ways, based on the solution of Eq. (3) for different initial conditions. The method used in the experiments conducted here is described next. Equation (3) provides the basis for determining  $\lambda$ :

$$\lambda = \frac{p(t) - p'(t)}{dp'(t)/dt} \quad (4)$$

This technique can be used to significantly accelerate the mapping of a flowfield, through on-the-fly data acquisition. The actual pressure  $p(t)$  can be measured as the probe sweeps through the area of interest. In other words, the probe need not stop at a point and wait for pressure  $p'(t)$  to reach steady state. Through this technique, one can also measure the actual pressure  $p(t)$  in a unsteady flowfield since one can calculate  $p(t)$  from  $p'(t)$  if the lag constant  $\lambda$  of the particular tubing assembly in use is known. However, the bandwidth that can be resolved through the technique is limited. Following the work of Whitmore and Moes,<sup>4</sup> one can see that a rigorous criterion that must be satisfied for the first-order model [Eq. (3)] to be valid is given (for moderate or short tubing lengths) by

$$\omega \ll 32\mu/d^2\rho_0 \quad (5)$$

where  $\omega$  is the radian frequency of the flow unsteadiness and  $\rho_0$  is the density. Let us consider an example involving the miniature multihole probes for which the algorithm was developed. The size of these probes is small for minimum intrusiveness, especially in intrusion-sensitive flows. In these probes, tubing i.d. of 0.25 mm are typical. For such diameters and typical density and viscosity values, we get, from Eq. (5),  $\omega \ll 7500$  rad/s. So, if we take  $\omega$  to be one order of magnitude smaller than 7500 rad/s, this translates to a frequency of 120 Hz. This is sufficient for many unsteady-flow-measurement applications and can yield very small wait times in flow surveys.

### IV. Experimental Setup

Figure 1 shows the schematic of the experimental setup used. A pressure pulse generator (PPG) is used to apply the transient pressure signal  $p(t)$  to one end of the pressure tubing. This pressure is measured directly by pressure transducer T1, and the other end of the pressure tubing is connected to the pressure transducer T2.

The pressure source (PPG) represents a flowfield. The pressure sensed by transducer T1 simulates the pressure at the tip of the probe, and that measured by transducer T2 simulates the pressure measured by the pressure transducer the probe is connected to. Any tubing assembly of interest can be inserted between junction A and transducer T2, and its equivalent lag constant  $\lambda$  can be determined. The operation principle of the PPG is described in Ref. 5.

Data acquisition was performed by a DAS-16 Jr A/D board (Computer Boards). The outputs from transducers T1 and T2 (Validyne) were fed into two channels of the board, and data acquisition was performed sequentially and not simultaneously. To minimize the error caused by this, the data were acquired at a sampling rate of 40,000 samples/s. Only the samples taken at every millisecond (for example, samples 1 and 2, then samples 41 and 42, then 81 and 82, and so forth) were retained and used for further analysis. The pressure transducers were regularly calibrated. A five-point calibration was performed, which accounted for transducer nonlinearities and thermal drifts. The reference manometer used for calibration had an uncertainty of 0.005 torr for the range of pressures used here ( $\pm 6$  torr). The preceding calibration, along with a one-count A/D conversion uncertainty, yielded a pressure measurement uncertainty of 0.010 torr. To render the pressure applied at junction A, a smoother function of time, a damper tube was introduced between the PPG outlet and junction A (Fig. 1). Moreover, to reduce the noise in the calculation of the pressure time derivative, a digital filter (running average) was first applied to the acquired data. The lag constant  $\lambda$  for the tubing system was then determined from Eq. (4).

### V. Results

Typical pressure signals  $p(t)$  and  $p'(t)$  are shown in Fig. 2 for a single actuation of the PPG. These data correspond to a simple tubing assembly, consisting of a single straight tube 18.5 in. (0.47 m) long with constant inside diameter of 0.010 in. (0.25 mm). Equation (4) was used to calculate a  $\lambda$  value of 0.862. As stated earlier, there is a time lag between  $p'(t)$  and  $p(t)$ . In other words, the pressure at transducer T2 takes some time  $\Delta t$  to reach the 99% of the steady-state pressure value. For the particular tubing used, the time lag was  $\Delta t = 3.877$  s, which would be a significant wait time in flow-mapping experiments.

Once the value of  $\lambda$  is calculated, we can calculate the corrected pressure  $P_{\text{corr}}(t)$  from the measured pressure  $p'(t)$  from the equation

$$P_{\text{corr}}(t) = p'(t) + \lambda \frac{dp'(t)}{dt} \quad (6)$$

This should be equal to the applied pressure  $p(t)$ . Figure 2 shows good agreement between  $P_{\text{corr}}(t)$  and  $p(t)$ . The average error was 0.007 torr. Subsequently, and for validation purposes, an arbitrary pressure signal  $p(t)$  was generated by repeated random actuations of the PPG. The two pressure signals  $p(t)$  and  $p'(t)$  were measured and

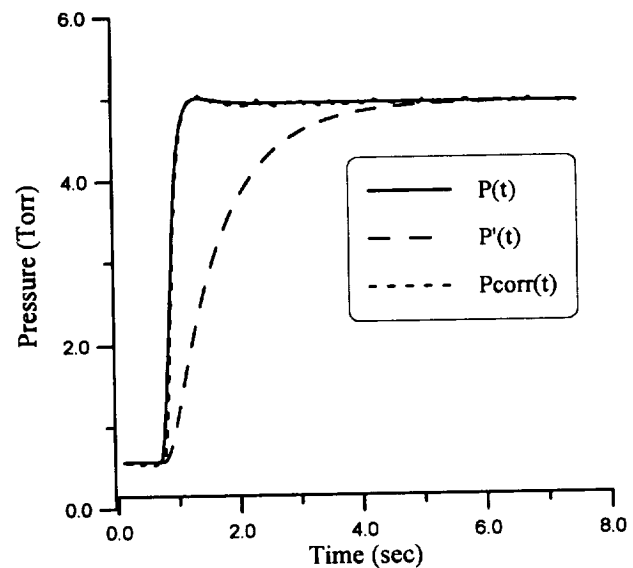


Fig. 2 Response of transducers T1 and T2 for a tubing of length 18.5 in. (0.47 m) and inner diameter of 0.010 in. (0.25 mm) for a single PPG actuation and corrected pressure  $P_{\text{corr}}(t)$ .

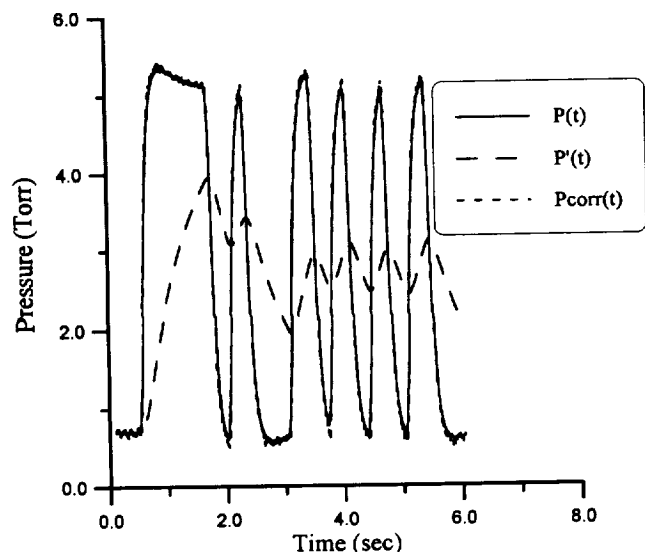


Fig. 3 Response of transducers T1 and T2 for the tubing corresponding to Fig. 2 for a series of random PPG actuations and corrected pressure  $P_{\text{corr}}(t)$ .

are shown in Fig. 3. From the already calculated value of  $\lambda$  ( $=0.862$ ) and pressure signal  $p'(t)$  measured by transducer T2, the corrected pressure  $P_{\text{cor}}$  was calculated and should reconstruct  $p(t)$ . As seen in Fig. 3, the agreement is excellent. For application of the technique to actual real-time flow measurements, the reader is referred to Ref. 5.

## VI. Conclusion

A simple technique was developed for pressure measurements in unsteady flows and on-the-fly data acquisition in steady flows using conventional pressure-sensing methods. This technique provides a means of compensating for the errors caused by pressure lag and attenuation in the pressure tubing, is computationally very inexpensive, and is implemented in real time. It is, however, limited to critically damped or overdamped tubing systems. The agreement of predicted and actual pressures validates the simple mathematical model for the tubing and the algorithm used to predict the actual applied pressure. This technique will help to bridge the gap until new pressure-sensing techniques are developed based on the incorporation of microelectromechanical systems pressure transducers on or near the surface of the probe tip. This development is currently undertaken by our group.

## Acknowledgments

This work was supported by the NASA Langley Research Center, Flow Modeling and Control Branch, William Sellers, Monitor, under Grant NAG-1-1753, and by Aeroprobe Corporation, under Project 32525-52050.

## References

- <sup>1</sup>Whitmore, S. A., and Leondes, C. T., "Pneumatic Distortion Compensation for Aircraft Surface Pressure Sensing Devices," *Journal of Aircraft*, Vol. 28, No. 12, 1991, pp. 828-836.
- <sup>2</sup>Huston, W. B., "Accuracy of Airspeed Measurements and Flight Calibration Procedures," NACA Rept. 919, Feb. 1948.
- <sup>3</sup>Wildhack, W. A., "Pressure Drop in Tubing in Aircraft Instrument Installations," NACA TN-593, Feb. 1937.
- <sup>4</sup>Whitmore, S. A., and Moes, T. R., "The Effects of Pressure Sensor Acoustics on Airdata Derived from a High-Angle-of-Attack Flush Airdata Sensing (HI-FADS) System," NASA TM-101736, Feb. 1991.
- <sup>5</sup>Pathak, M., "A Simple Technique for Frequency Response Enhancement of Miniature Pressure Probes," M.S. Thesis, Aerospace Engineering Dept., Texas A&M Univ., College Station, TX, Dec. 1998.

R. P. Lucht  
Associate Editor

# **APPENDIX C**



# THE COMPRESSIBLE CALIBRATION OF MINIATURE MULTI-HOLE PROBES

Espen S. Johansen<sup>†</sup>  
Department of Mechanical Engineering  
Texas A&M University, College Station, Texas

Othon K. Rediniotis<sup>\*</sup>  
Department of Aerospace Engineering  
Texas A&M University, College Station, Texas

Greg Jones<sup>\*</sup>  
Flow Modeling and Control Branch  
NASA Langley Research Center, Hampton, Virginia

## ABSTRACT

This work presents the development of a data reduction algorithm for non-nulling, miniature, multi-hole pressure probes in compressible, subsonic flowfields. The algorithm is able to reduce data from any 5- or 7-hole probe and generate very accurate predictions of the velocity magnitude and direction, total and static pressures, Mach and Reynolds number. The algorithm utilizes a database of calibration data and a local least-squares interpolation technique. It has been tested on 4 novel miniature 7-hole probes that were fabricated at the Aerospace Engineering Department of Texas A&M University and calibrated at the NASA Langley Flow Modeling and Control Branch for the entire subsonic regime. Each of the probes was miniature in size with a tip diameter of 0.065". Extensive uncertainty analysis of the calibration procedures and the data reduction algorithm was performed. Excellent prediction capabilities are demonstrated with prediction uncertainties less than 0.2 degrees in angle prediction and less than 0.35% in velocity magnitude prediction.

<sup>†</sup> : Graduate Research Assistant, Student Member AIAA  
<sup>\*</sup> : Assistant Professor, Member AIAA  
<sup>✱</sup> : Research Scientist, NASA Langley Research



## NOMENCLATURE

$a_0, a_1, a_2$	=	Polynomial constants calculated by least-squares method
$A_t, A_s$	=	Non-dimensional total and static pressure coefficients
$b_1$	=	Non-dimensional pitch or cone pressure coefficient
$b_2$	=	Non-dimensional yaw or roll pressure coefficient
$d$	=	Euclidean distance from calibration point to test point
$Ma$	=	Mach number
$\hat{n}$	=	Directional unit vector
$N$	=	Number of calibration points used by local least-squares interpolation
$p$	=	Pressure
$q$	=	Pseudo-dynamic pressure
$R$	=	Universal gas constant
$Re$	=	Reynolds number
$T$	=	Temperature
$U$	=	Velocity magnitude
$u, v, w$	=	Cartesian velocity components
$\vec{V}$	=	Velocity vector
$w$	=	Interpolation weight
$\alpha$	=	Pitch angle
$\beta$	=	Yaw angle
$\phi$	=	Roll angle
$\theta$	=	Cone angle
$\lambda$	=	Offset angle for port orientation
$\rho$	=	Density
$\mu$	=	Viscosity

### Subscripts

$\alpha, \beta$	=	Pitch, yaw
$\theta, \phi$	=	Cone, roll
$C$	=	Calibration
$compr$	=	Compressible
$i$	=	Port with maximum pressure
$j$	=	Calibration point number in calibration database
$s$	=	Static
$t$	=	Total
$T$	=	Test

### Superscripts

$+$	=	In the clockwise direction looking into the probe tip
$-$	=	In the counter-clockwise direction looking into the probe tip

### Abbreviations

LLS	=	Local Least-Squares
PIV	=	Particle Image Velocimetry
LDV	=	Laser Doppler Velocimetry



FSO = Full Scale Output  
ESP = Electronic Pressure Scanner ©Pressure Systems Inc.

## INTRODUCTION

The multi-hole pressure probe is a cost effective, robust and accurate instrument for three-dimensional velocity and pressure measurements in a wide range of flowfields. For steady-state measurements, 5- and 7-hole probes are capable of resolving flow angularities up to approximately 75 degrees and predict the flow conditions with high accuracy. Although powerful, measurement techniques such as Laser Doppler Velocimetry (LDV) and Particle Image Velocimetry (PIV) have a number of disadvantages compared to multi-hole probes. LDV and PIV require the use of costly components, such as expensive lasers and optical equipment. Both methods are complex and require painstaking alignment of lasers and optical equipment to obtain accurate flow measurements, and it is often hard to get good results outside the laboratory environment.

A calibrated probe can be inserted into an unknown flowfield and accurately predict the velocity vector by recording the port pressures and comparing them with the calibration database through a set of non-dimensional coefficients. Historically, a number of different calibration techniques have been utilized for multi-hole probes, all with their own advantages and difficulties. A commonly used method for hemispherical probe tips has been to apply the potential flow equations for a sphere to relate the flow angles and velocity magnitude to the pressure differentials measured on the probe tip. Kjelgaard<sup>1</sup> used this technique on a hemispherical tipped 5-hole probe. This approach is sensitive to construction defects of the probe tip. Multi-hole probes are generally desired to be small in size such that the flow disturbance caused by the probe can be kept to a minimum. When minimizing the probe tip dimensions, construction imperfections become increasingly inevitable and the relative impact of the imperfections on the probe response is also



increasing. Pressure distributions based on a theoretical model are inaccurate because of discrepancies between the theoretical probe geometry and the physical probe. To compensate for the manufacturing defects, each probe has to be calibrated individually using extensive calibration routines. To account for compressibility and viscous effects, probes are also often calibrated over a range of Mach and Reynolds numbers.

One method of calibrating multi-hole probes is to insert the probe into a flowfield of known magnitude and direction. The probe is then pitched and yawed through a range of known angles, to simulate every possible measurable velocity inclination. For each such probe orientation, the pressures from all the pressure ports are recorded and stored in a database. Angle increments are typically 0.5 to 5 degrees yielding a database with several thousand data points, each with a pressure signature that is unique for that angle inclination and velocity magnitude. Unless the probe is physically damaged it will keep its characteristics and only one calibration is required for the lifetime of the probe.

Several methods of comparing the measured pressures from an unknown test case with the calibration database have been developed. Bryer and Pankhurst<sup>2</sup> applied relationships derived from a set of pressure coefficients over the different flow regions of the probe. On a 5-hole probe the measurement domain of the probe was divided into one low-angle regime and four high-angle regimes corresponding to the center port and each of the peripheral ports, respectively. The calibration data was used to derive empirical relationships expressing the angle inclinations and the magnitude of the velocity vector in terms of the measured pressure coefficients. Rediniotis et al.<sup>3</sup> derived polynomial fits for calibration data for conical 7-hole probes. Further they divided the port specific regions into several sections thus increasing the number of regions for which polynomials were used to describe the flow variables. They created 8 regions describing the low angle flow



(where the center port senses the highest pressure) and 12 high angle regions (where any of the 6 peripheral ports senses the highest pressure). The method of subdividing the regions increased the goodness of the polynomial fit through the calibration points, but did not necessarily ensure well-behaved calibration surfaces between data points.

The polynomial fit techniques mentioned are global in nature, that is they generate polynomial fits for relatively large sectors or regions. Though Rediniotis et al.<sup>3</sup> reduced the region size by subdividing the sectors, the individual regions were still large and could, depending on the density of the calibration data, contain hundreds of data points. Using polynomial fits for large regions can cause the overall prediction accuracy to decline because of the large number of calibration points the fit tries to model. Utilizing a local interpolation scheme instead of a region-wide polynomial fit has also been used with multi-hole probe calibration methods. Zilliac<sup>4</sup> calibrated conical tipped 7-hole probes for use in flowfields with high angularity. For each of the calibration points, the seven port pressures, the total pressure and the known pitch and yaw angles were recorded in a database. Sets of non-dimensional pressure coefficients were also stored in the calibration database. For a calibrated probe in an unknown flowfield the seven port pressures were recorded and the non-dimensional coefficients calculated. By searching the calibration database for similar coefficient values the approximate flow conditions were identified. Adjacent coefficient values were interpolated to solve for intermediate angles and pressure coefficient values. The accuracy of this technique is dependent on the density of the calibration data. In the present work, the data-reduction algorithm has similarities to that of Zilliac's; however new features have been introduced that have allowed us to push the prediction uncertainties to very low levels, as it will be seen in the uncertainty analysis discussion.



Four miniature 7-hole probes were designed and built. They were subsequently calibrated at the NASA Langley Flow Modeling and Control Branch. The work presented herein describes the calibration and data reduction procedures, Mach and Reynolds number effects on the calibration and a detailed uncertainty analysis.

## **FACILITY AND PROBE DESCRIPTION AND EXPERIMENTAL PROCEDURES**

The four miniature 7-hole probes were identical and their design is illustrated in figure 1. It is worth-noticing that the probe tip diameter was only 0.65". The back of the probe was formed into a bullet-shape afterbody to minimize unsteady vortex-shedding effects. Each one of the ports on the probe tip communicates, through internal tubing and a 90-degree elbow, with one of the stainless steel connecting tubes (figure 1). All probes were calibrated at the NASA LaRC Probe Calibration Tunnel (PCT). This facility is a variable density pressure tunnel that can independently control Mach number, Reynolds number, and total temperature. The PCT configuration for 7-hole probe calibration is shown in figure 2. This open return tunnel is supplied from a 5000 psi bottle field and exhausts into either a baffled atmospheric trench or vacuum sphere. The air is preheated with a steam heater to compensate for the gross Joule Thompson temperature effects. A secondary electric heating system is used to set the final tunnel total temperature. The interaction of the temperature and pressure systems is dependent on the mass flow through the system. The tunnel operator selects the mode of operation to maintain Mach number variations less than 1% of set value, tunnel pressure variations less than 0.1 psi, and tunnel temperature variations less than 1°F. If at any time the tunnel conditions deviate more than these tolerances, the probe data acquisition process is paused, then resumed when the conditions are reestablished. The test envelope for the calibration is shown in figure 3. The four probes were calibrated at Mach numbers ranging from 0.1



to 0.8, in increments of 0.1, and at free-stream total pressure of 17, 32 and 60 psi which yield a Reynolds number (per unit length) range from  $2.5 \cdot 10^6 \text{m}^{-1}$  to  $52 \cdot 10^6 \text{m}^{-1}$ . In figure 3, each of the curves represents a different wind tunnel total pressure during the calibration.

Each probe was calibrated by inserting it into a flowfield of known properties. The probe was mounted on a traversing system capable of pitching and yawing the probe, as shown in figure 2. While the flow magnitude and direction stays constant the probe is pitched and yawed through a set of known angles relative to the flow direction, keeping the location of the probe tip fixed on the axis of the tunnel nozzle from which the calibration jet flow emanates. For each of these sets of angles all of the port pressures from the probe were recorded. The traversing system consisted of two stepper motors that could vary the probe pitch and yaw angles within the range  $-60$  degrees to  $+60$  degrees, in 2 degree increments. Each stepper motor was equipped with an optical encoder that provided probe positioning feedback with an accuracy of 0.01 degrees. The pressures were measured using four different ESP pressure scanner units from PSI Inc. Depending on the pressure range experienced at a specific calibration, the ESP unit with the proper pressure range was used. This “staging” of the ESP units allowed us to achieve significantly higher pressure measurement accuracy than if one single ESP unit with a large pressure range were used. The specific ESP ranges and the achieved accuracies are discussed in the uncertainty analysis section.

## **LOCAL LEAST-SQUARES DATA REDUCTION ALGORITHM**

Two different sets of angles are used to describe low-angle and high-angle flow (Gerner and Maurer<sup>5</sup>), pitch and yaw angles ( $\alpha$ ,  $\beta$ ) and cone and roll angles ( $\theta$ ,  $\phi$ ), respectively. These two sets of angles are shown in figure 4. The conversion from the pitch and yaw angles to the cone and roll angles is given by:



$$\theta = \cos^{-1}(\cos \alpha \cdot \cos \beta) \quad (1)$$

$$\phi = \tan^{-1}\left(\frac{\tan \alpha}{\sin \beta}\right) \quad (2)$$

Each sector on the face of the probe (figure 5) is identified by the pressure port that senses the highest pressure for all possible flow inclinations within that sector. The flow over a 7-hole probe is divided into low-angle and high-angle flow regimes. Low-angle flow is identified when pressure port 1, the central port, has the highest pressure. High-angle flow is identified when the highest pressure occurs in one of the peripheral ports 2 through 7. In figure 5,  $\lambda$  is the offset-angle that defines the roll orientation of the pressure port pattern relative to a physical reference surface on the probe, and is used by the data reduction algorithm. In this case, the reference surface is a flat surface on the top side of the probe, immediately upstream of the bullet-shape afterbody.

The local velocity vector at any measurement location can be fully characterized by four variables. For low-angle flow these variables are: pitch angle  $\alpha$ , yaw angle  $\beta$ , total pressure coefficient  $A_t$  and static pressure coefficient  $A_s$ . For high-angle flow the variables are: cone angle  $\theta$ , roll angle  $\phi$ ,  $A_t$  and  $A_s$ . As mentioned above, knowledge of the local total temperature is also required, which for this work has been considered constant and equal to the free-stream temperature. These four quantities need to be determined as functions of two non-dimensional pressure coefficients formed from the 7 measured pressures:  $b_\alpha$ ,  $b_\beta$  for low-angle flow and  $b_\theta$ ,  $b_\phi$  for high-angle flow (Rediniotis et al.,<sup>3</sup> Everett et al.<sup>6</sup>).

For a 7-hole probe, in the low-angle flow regime (sector 1) the following definitions are used:

$$b_\alpha = \frac{1}{\sqrt{3}} \cdot \frac{(p_7 + p_5 - p_4 - p_6)}{q} \quad (3a)$$



$$b_{\beta} = \frac{(p_2 - p_3)}{q} + \frac{(p_6 - p_5 + p_7 - p_4)}{2 \cdot q} \quad (3b)$$

$$A_t = \frac{(p_1 - p_t)}{q} \quad (3c)$$

$$A_s = \frac{q}{(p_t - p_s)} \quad (3d)$$

The pseudo-dynamic pressure,  $q$ , is defined as:

$$q = p_1 - \frac{(p_2 + p_3 + p_4 + p_5 + p_6 + p_7)}{6} \quad (3e)$$

For a 7-hole probe, in the high-angle flow regime (sectors 2-7) the following definitions are used:

$$b_{\theta} = \frac{(p_i - p_1)}{q} \quad (4a)$$

$$b_{\phi} = \frac{(p^+ - p^-)}{q} \quad (4b)$$

$$A_t = \frac{(p_i - p_t)}{q} \quad (4c)$$

$$A_s = \frac{q}{(p_t - p_s)} \quad (4d)$$

The pseudo-dynamic pressure,  $q$ , is defined as:

$$q = p_i - \frac{(p^+ + p^-)}{2} \quad (4e)$$

In the previous definitions,  $p_i$  is the highest measured pressure (at the  $i^{\text{th}}$  port). Looking into the probe tip,  $p^+$  and  $p^-$  are the pressures measured by the peripheral holes adjacent to port  $i$ , in the clockwise and counter-clockwise direction, respectively. The input coefficients  $b_{\alpha}$ ,  $b_{\theta}$  will be referred to as  $b_1$  and  $b_{\beta}$ ,  $b_{\phi}$  will be referred to as  $b_2$  in the remainder of this text, since many of the



processes described below use both high- and low-angle definitions in the same manner. In the description of the local least-squares data reduction algorithm, the 7-hole definitions will be used; however the same principles apply to the 5-hole probe definitions.

In a preprocessing procedure, the probe calibration files are used to create a new calibration database that contains, for all velocity inclinations, all of the non-dimensional coefficients defined in equations 3 and 4. A global scaling factor,  $\Delta b_2/\Delta b_1$ , is introduced to bring the coefficient scales on the same order of magnitude and thus improve 2D interpolation based on Euclidean distances in the  $b_1$ - $b_2$  plane. This factor is defined using the maximum and minimum values of the coefficients found in the calibration file, and is stored in the calibration database:

$$\frac{\Delta b_2}{\Delta b_1} = \frac{(b_{2C})_{\max} - (b_{2C})_{\min}}{(b_{1C})_{\max} - (b_{1C})_{\min}} \quad (5)$$

When the probe is inserted into an unknown flowfield, 7 port pressures are recorded and the non-dimensional coefficients  $b_1$  and  $b_2$  are calculated. That is  $b_\alpha$  and  $b_\beta$  for low-angle flow and  $b_\theta$  and  $b_\phi$  for high angle flow. The second step is to find the closest values of the independent coefficients in the calibration file compared to the test values. The closest data points are found in terms of Euclidean distance:

$$d_j = \sqrt{\left(\frac{\Delta b_2}{\Delta b_1} \left( (b_{1C})_j - b_{1T} \right)\right)^2 + \left( (b_{2C})_j - b_{2T} \right)^2} \quad (6)$$

Where the index  $j$  indicates a specific calibration point and  $d_j$  is the Euclidean distance, in the  $b_1$ - $b_2$  plane, from the coefficients of the test point,  $(b_{1T}, b_{2T})$ , to the scaled (using equation 5) coefficients of the  $j$  calibration point,  $(b_{1C}, b_{2C})_j$ .

It is necessary that the selected calibration points  $(b_{1C}, b_{2C})$  be distributed around the test point  $(b_{1T}, b_{2T})$  to obtain a well-behaved polynomial surface and allow for interpolation rather than extrapolation. A procedure checks if the closest calibration points, in triplets, form triangles



enclosing the test point in the b1-b2 plane. The original ranking of the closest points based on the Euclidean distance,  $d_j$ , can be altered to ensure that (if at all possible) the combination of the closest calibration points forms triangles around the test point. The algorithm will search for a minimum of two such triangles. In figure 6, the star indicates the test point ( $b1_T, b2_T$ ) and the circles at the corners of the triangles indicate the closest selected calibration points ( $b1_C, b2_C$ ) that have also been checked for the triangulation requirement. Whether a test point (point P in figure 7) is enclosed by a certain triangle formed by three calibration points (points A, B and C in figure 7) is checked by first calculating the unit vectors  $\hat{n}_1$ ,  $\hat{n}_2$  and  $\hat{n}_3$ ,

$$\hat{n}_1 = \vec{AP} \times \vec{AC} \quad (7a)$$

$$\hat{n}_2 = \vec{CP} \times \vec{CB} \quad (7b)$$

$$\hat{n}_3 = \vec{BP} \times \vec{BA} \quad (7c)$$

If all 3 vectors have the same direction the test point P is within the triangle, otherwise P is outside the triangle.

In some cases, like the one illustrated by figure 8, a test point might be lying close to the boundary between sectors (sectors 3 and 5 in figure 8). In figure 8, the diamond indicates the test point, the circles indicate the calibration points, and the boundaries between adjacent sectors are indicated by the thick solid lines. Since the algorithm searches for the closest calibration points that also satisfy the triangulation requirement around the test point, in this case it will have to choose calibration points from both sectors (3 and 5). A procedure was introduced to allow the algorithm to do that. As described above, this selection is based on the values of coefficients b1 and b2. However, the coefficient definitions for b1 and b2 are sector-sensitive. In order to make the coefficients ( $b1_C, b2_C$ ) of calibration points from different sectors comparable, the adjacent sectors



use the coefficient definitions for  $b_1$ ,  $b_2$  of the primary sector (sector that senses the maximum pressure). A decision as to whether a test point is close enough to the boundary between two sectors (and therefore the algorithm would have to consider calibration points from both sectors) is made by the algorithm based on whether or not the test point is within the “overlap” region between the two sectors. This “overlap” region is defined as the locus of all points for which the pressures of the two ports corresponding to the two sectors differ by less than a user-specified percentage of the maximum port pressure. Let us consider an example based on figure 8. Port 3 has the maximum pressure, for example 10.0 Torr, and the user has defined an “overlap” percentage of 25 %. Then, if port 5 senses a pressure of 8.0 (which differs from the maximum pressure less than 25 % of the maximum pressure), the algorithm decides that the test point lies close to the boundary between sectors 3 and 5, and will in this case consider calibration points from both sectors, 3 and 5, for the local interpolation.

Calibration points far from the tested point (in the  $b_1$ - $b_2$  plane) are assumed to have little or no influence on the calculation. Therefore, a local interpolation scheme is used and only calibration points close to the test point are used in the evaluation. A least-squares surface fit technique is used to calculate the two flow angles and the two pressure coefficients as functions of the input variables,  $b_1$  and  $b_2$ . The selected closest and triangulation-checked calibration points (minimum number determined by the order of the polynomial interpolation surface) are used to calculate 4 separate interpolation surfaces. Each surface is represented as a polynomial with coefficients calculated by a least-squares approximation method. For a planar surface the following polynomial is used to describe the surface:

$$f(b_1, b_2) = a_0 + a_1 \cdot b_1 + a_2 \cdot b_2 \quad (8)$$



Where  $f$  can be any of the variables  $\alpha$ ,  $\beta$ ,  $\theta$ ,  $\phi$ ,  $A_t$ ,  $A_s$  and  $a_0$ ,  $a_1$ ,  $a_2$  are the least-squares polynomial coefficients. By entering the measured input coefficients ( $b1_T$ ,  $b2_T$ ) into the calculated function  $f(b1, b2)$ , interpolated values for  $\alpha_T$ ,  $\beta_T$ ,  $\theta_T$ ,  $\phi_T$ ,  $(A_t)_T$  and  $(A_s)_T$  are obtained. The angle or pressure coefficient surfaces for the probe are assumed to be smooth locally and not exhibit any large gradients or discontinuities. The local least-squares method generates a surface that does not directly go through all the selected calibration data points, but is rather an average surface. A standard polynomial surface fit can exhibit large fluctuations because the surface is required to go through all the data points. The least-squares surface will moderate the effect of a badly selected or measured point and create the best overall surface fit.

The total and static pressures are calculated from the non-dimensional pressure coefficients  $(A_t)_T$ ,  $(A_s)_T$ :

$$p_t = p_i - (A_t)_T \cdot q_T \quad (9a)$$

$$p_s = p_t - \frac{q_T}{(A_s)_T} \quad (9b)$$

In equations 9a and 9b the pressure  $p_i$  is the port with maximum pressure and  $q_T$  is the pseudo-dynamic pressure for the test point (from equation 3e or 4e). The velocity magnitude and the flow conditions are calculated using adiabatic, perfect gas relationships for air<sup>7</sup>. The Mach number is calculated from:

$$Ma = \sqrt{(5 \cdot (e^{(-2/7 \cdot \ln(p_i/p_t))} - 1))} \quad (10)$$

Temperature, compressible dynamic pressure and density are given by:

$$T = \frac{T_t}{(1 + M^2/5)} \quad (11)$$

$$q_{compr} = 0.7 \cdot p_s \cdot Ma^2 \quad (12)$$



$$\rho = \frac{P_s}{R \cdot T} \quad (13)$$

Where R is the universal gas constant (287 J/kg·K).

The velocity magnitude is calculated by:

$$U = \sqrt{\frac{2 \cdot q_{compr}}{\rho}} \quad (14)$$

The Cartesian velocity components for low-angle flow are then given by:

$$u = U \cdot \cos \alpha \cdot \cos \beta \quad (15a)$$

$$v = U \cdot \cos \alpha \cdot \sin \beta \quad (15b)$$

$$w = U \cdot \sin \alpha \quad (15c)$$

while the Cartesian velocity components for high-angle flow are given by:

$$u = U \cdot \cos \theta \quad (16a)$$

$$v = U \cdot \sin \theta \cdot \cos \phi \quad (16b)$$

$$w = U \cdot \sin \theta \cdot \sin \phi \quad (16c)$$

The air viscosity  $\mu$  is derived from Sutherland's law, and the Reynolds number per unit length is:

$$\frac{Re}{l} = \frac{U \cdot \rho}{\mu} \quad (17)$$

The data reduction procedure described above is repeated for each separate test data point.

## COMPRESSIBILITY AND VISCOSITY EFFECTS

As previously mentioned the probes were calibrated for a wide range of Mach and Reynolds numbers. In this section, we present the results on the calibration dependence on Mach and Reynolds numbers and discuss the algorithms capability to take these effects into account. Previous work has shown that the non-dimensional coefficients b1 and b2 have a slight dependence on Mach



and Reynolds number (Krause and Dudzinski,<sup>8</sup> Ainsworth et al.,<sup>9</sup> Dominy and Hodson<sup>10</sup>). The non-dimensional coefficients dependence on Mach and Reynolds number, derived from our calibration data, are shown in figures 9 to 12. The observed ranges of values for the pressure coefficients  $b_1$  and  $b_2$  are 0 to 1.7 and  $-2$  to 2, respectively, and the ranges for the pressure coefficients  $A_t$  and  $A_s$ , are  $-0.8$  to 0 and 0 to 1.4 respectively. The data in figures 9 to 12 refer to calibration points with the same flow angles, i.e. cone angle of 25 degrees and roll angle of 84 degrees. However similar behavior is exhibited at any angle within the measurable regime. As seen in figures 10 and 12 the calibration dependence on Reynolds number is very small, and the dependence on Mach number is fairly small, however not negligible if accurate measurements are expected. It should be pointed out here that the apparently non-negligible dependence of the calibration on Reynolds number (figures 10 and 12) at  $Ma=0.1$ , is most likely an artifact of the rather poor accuracy in the pressure measurements at that specific, low Mach number, as it will be further discussed in the uncertainty analysis section. From figures 9 and 10, it can also be seen that the dependence of  $b_1$  on  $Ma$  is stronger than that of the dependence of  $b_2$  on  $Ma$ . Also, the dependence of  $A_t$  and  $A_s$  on  $Ma$  and  $Re$  (figures 11 and 12) is stronger than the dependence of  $b_1$  and  $b_2$  on  $Ma$  and  $Re$  (figures 9 and 10). This means that if no  $Ma$  and  $Re$  effects are taken into account in the data reduction process, the prediction of the velocity magnitude is likely to suffer most.

Below we discuss how the algorithm takes into account Mach and Reynolds number effects. Since the dependence is small, the pressures measured by the probe in an unknown flowfield can be used with a calibration file from any Mach and Reynolds number to estimate the angles within a few degrees and the velocity magnitude within a few percent. Approximate values for the Mach and Reynolds numbers for the flow are also obtained. Reducing test data with a calibration file from the same flow conditions (same  $Ma$  and  $Re$  numbers) will yield the most accurate predictions, thus to



obtain high prediction accuracy throughout the entire subsonic regime, it is necessary to calibrate the probe over a wide range of Mach and Reynolds numbers. By reducing test data from an unknown flowfield with a range of calibration files, it is possible to find the best-predicted flow conditions by proper interpolation between the results from the separate files. Everett et al.<sup>6</sup> introduced a compressibility coefficient to correct for the Mach number effects. A similar approach was initially attempted here using a compressibility coefficient in conjunction with the interpolation based on the coefficients b1 and b2. No consistent prediction accuracy was achieved with this method. Thus in the luxury of having the probes calibrated at a wide range of Mach and Reynolds numbers in small increments a data reduction based solely on the coefficients b1 and b2 was chosen. The algorithm creates a probe specific database using any number of calibration files, and reduces a test point from an unknown flowfield with all of the calibration files provided in the database and stores the predicted values from each of these data reductions. Average predicted Mach and Reynolds number are then calculated and the differences between these and the Mach and Reynolds number in the individual calibration files are used to calculate an interpolation function. This function gives the final results based on interpolation between the predicted values from the closest files in terms of Mach and Reynolds number. The interpolation function is given by:

$$w_i = \frac{\prod_{j=1}^N d_{j \neq i}^P}{\sum_{k=1}^N \prod_{j=1}^N d_{j \neq k}^P} \quad (18)$$

Where N is the number of files used in the interpolation,  $w_i$  are the individual weights for each of the N files,  $d_j$  is the Euclidean distance between the average predicted Mach and Reynolds number and the Mach and Reynolds in each of the separate files. P is an exponent to increase the sensitivity and enforce mostly use of the files that are closest in terms of the Euclidean distance in the Ma-Re



plane. The final values are calculated by using the individual weights multiplied with the predicted values from each of the closest N files:

$$f_{\text{final}} = \sum_{i=1}^N (w_i \cdot f_i) \quad (19)$$

Where  $f_{\text{final}}$  is any of the final estimates for the two flow angles and the pressure coefficients  $A_t$  and  $A_s$ , and  $f_i$  ( $i=1, \dots, N$ ) are the predicted quantities from each of the N closest files.

## UNCERTAINTY ANALYSIS

The uncertainty analysis presented below is based on the techniques discussed in Moffat<sup>11</sup>. To find the uncertainties of the local least-squares data reduction algorithm an extensive analytical and numerical analysis was performed. The procedures to determine the uncertainty of the algorithm consisted of:

- A combined analytical and numerical analysis of how uncertainties in the pressure measurements propagate through the algorithm
- Evaluation of the uncertainty of the LLS surface fitting procedure
- Evaluation of the uncertainty of the algorithm using data verification test

Attention should also be directed to the problem of bias or systematic error, which is error that is roughly constant throughout the sampling of the data. Such errors can be due to errors in the reading of the reference manometer, hysteresis and temperature drift of the pressure transducers and errors in probe positioning. Extreme care was taken, during probe calibration, to eliminate all bias errors.

First, the uncertainty of the pressure measurements was estimated. Taking into account the pressure scanner (ESP from PSI Inc.) specifications, the frequency and type of transducer calibration, the reference manometer uncertainty and the A/D conversion uncertainty, the pressure



measurement uncertainty was estimated and is presented in figure 13. As seen in this figure, the pressure measurement uncertainty was highest at Ma=0.1 (dynamic pressure q less than 0.3 psi). At all other conditions the uncertainty was from twice to ten times smaller than the uncertainty at Ma=0.1. As it was previously discussed, this increased uncertainty at Ma=0.1 is suspected to be the reason for the observed Reynolds number dependence of the calibration at Ma=0.1 (figures 10 and 12). Errors in probe positioning were negligible, since both pitch and yaw positioning mechanisms were equipped with optical encoders that ensured an accuracy of 0.01 degrees.

### Analysis of Error Propagation through the Algorithm

Two different approaches are often used to estimate the uncertainty, the worst-case approach or the constant-odds approach. In the present analysis the constant-odds approach is followed. The uncertainty  $\delta R$  of a function  $R$  that depends on  $n$  independent variables  $x_i$ , with associated uncertainty  $\delta x_i$ , is given by:

$$\delta R = \left[ \left( \frac{\partial R}{\partial x_1} \delta x_1 \right)^2 + \left( \frac{\partial R}{\partial x_2} \delta x_2 \right)^2 + \dots + \left( \frac{\partial R}{\partial x_n} \delta x_n \right)^2 \right]^{1/2} \quad (20)$$

The general form for constant-odds uncertainty prediction was given by Kline and McClintock<sup>12</sup>. This approach requires that each of the  $x_i$ 's be independent variables and that they have a Gaussian error distribution. Each of the coefficients ( $R = b_\alpha, b_\beta, b_\theta, b_\phi, A_t$  and  $A_s$ ) were differentiated with respect to the pressure terms ( $x_i = p_i$ ) they depend on. Based on equation 20, eight expressions were derived for the uncertainty of all non-dimensional pressure coefficients (four for low-angle flow:  $\delta b_\alpha, \delta b_\beta, \delta A_t$  and  $\delta A_s$ , and four for high-angle flow:  $\delta b_\theta, \delta b_\phi, \delta A_t$  and  $\delta A_s$ ).

In evaluating the propagation of uncertainty through the LLS algorithm, the ‘‘jitter’’ approach, as described in ref. 12, was employed. A modified version of the local least-squares data



reduction algorithm was created in order to evaluate the uncertainty propagation. It was assumed that the error in the pressure measurements is normally distributed. To generate perturbed (by the pressure measurement uncertainty) pressure values, a Gaussian distribution of pressure perturbations (errors) was created with zero mean and standard deviation equal to the pressure measurement uncertainty obtained from figure 13. The data reduction algorithm uses 6 local calibration data points to estimate one test point. The 7 port pressures for each of these 7 points (6 calibration points and 1 test point) were perturbed using random values from the pressure perturbation file. These perturbed pressures were subsequently used to calculate the uncertainties of all non-dimensional pressure coefficients, through the uncertainty expressions previously derived for those coefficients based on equation 20. These perturbed, non-dimensional coefficients are subsequently used by the LLS algorithm to generate perturbed interpolation surfaces. The reduction is executed and the results from the perturbed analysis are compared to the results from an unperturbed analysis. The uncertainty is defined as one standard deviation of the difference between the results obtained from the unperturbed analysis and the results obtained from the perturbed analysis (table 1). As it can be seen from table 1, no distinction was made between low-angle and high-angle flow in the evaluation of the angle uncertainty. In fact, as it will be shown later, the low-angle flow regime has angle uncertainties (pitch, yaw) significantly smaller than those in table 1.

### **Surface Fit Evaluation**

An estimation of the errors introduced from using a linear least-squares interpolation technique was performed. The surface fitting procedure in many conventional data reduction algorithms is found to be one of the greatest sources of error. A global surface fitting procedure will complicate the topology of the surface because the probe tip surface on a small probe usually



contains irregularities that will be reflected in the measured pressures and non-dimensional coefficients. Even smaller sector surfaces have these problems when trying to fit an interpolation surface to all calibration points in that sector, since each such sector might contain hundreds of calibration points. A local least-squares approach can be more accurate, since the surface is only covering a small segment of the calibration regime and uses only a few calibration data points. A linear local least-squares surface can create a very good approximation to the actual data assuming that there is a dense grid of calibration data.

A procedure to validate the accuracy of the LLS routine was performed using a known model surface (one model surface for each one of the dependent flow variables  $\alpha$ ,  $\beta$ ,  $\theta$ ,  $\phi$ ,  $A_t$ ,  $A_s$ ). For each of the separate sectors on a 7-hole probe, a sample/model least-squares surface was created using all the calibration data points belonging to that sector. A second order polynomial surface was created using least-squares surface fitting software. The resultant error ( $R^2$ ) of fitting a second order surface over all the calibration data points in each sector was reasonably good. The second order surface was now regarded as a model surface, since it contains similar characteristics to an actual calibration surface. Because the polynomial expression is known for the surface, a grid of non-dimensional coefficients ( $b_1$ ,  $b_2$ ) was created with corresponding exact values for the flow properties ( $\alpha$ ,  $\beta$ ,  $\theta$ ,  $\phi$ ,  $A_t$ ,  $A_s$ ). The new grid (simulated calibration grid) was created to have similar density and distribution of data points as a typical calibration database. A grid of test points was also created, with none of its points coincident with the points of the simulated calibration grid. For these test points, the exact values for the flow properties are also known. The new test file is reduced using a modified version of the LLS algorithm that uses the simulated calibration points. The error is calculated as the difference of the LLS calculated flow variables and the exact (known) flow variables for the test point, calculated by the polynomial expression for the model surface. The



data reduction also selects which calibration points to use in the data reduction such that this method can also serve as a measure for the quality of the calibration data point search and selection routine.

As previously discussed, the actual calibration surfaces are most probably not smooth 2<sup>nd</sup> order polynomial surfaces over an entire sector and they might exhibit larger curvature locally. Several “worst case” examples were analyzed by fitting a higher curvature surface through fewer data points. However, the results from this analysis showed that the contributing errors due to the local least-squares surface fit are negligible. Discrepancies between the fitted surface and the model surface were on the order of  $10^{-5}$  degrees for angle calculations and  $10^{-3}$  percent for velocity calculations.

### **Evaluating the LLS Algorithm Using Test Verification Files**

When calibrating multi-hole pressure probes a common practice is to record a separate test file with points not coinciding with the calibration data points. The pressures and the angles for the test points are recorded in the same manner as for the calibration points, such that they can be used for verification of the quality of the calibration and the data reduction algorithm. Several verification files from the probes calibrated at the PCT facility at NASA Langley were used to give a measure of the uncertainties expected when reducing an actual test data file. Error histograms, calculated for Probe 1 using a verification test data file, are presented here. The verification data file was recorded at  $Ma=0.5$  and  $Re= 11 \cdot 10^6 m^{-1}$ . The quality of the calibration and the data reduction is measured by the discrepancies between the angles and velocity magnitude in the verification file and the predicted angles and velocity magnitude. These discrepancies are referred to as the error ( $e$ ) and are presented in the histograms of figure 14. The error (its absolute value) is represented along



the horizontal axis, while the height of a histogram bar is proportional to the number of points in that specific error bin. This number is also indicated explicitly, over the bar. The uncertainty was subsequently derived by calculating the standard deviation of the error. The uncertainties calculated this way are listed in table 2. As seen from tables 1 and 2 there is good agreement between the calculated uncertainty and the measured uncertainty from the data verification files. As it was previously mentioned, one can see from Table 1 that the low-angle flow regime has angle uncertainties (pitch, yaw) significantly smaller than the high-angle flow regime angle uncertainties (cone, roll).

## CONCLUSIONS

The multi-hole pressure probe is a cost effective, robust and accurate method for determining the three-dimensional velocity vector and Ma and Re numbers in any unknown subsonic flowfield. For steady-state measurements 5- and 7-hole probes are capable of resolving flow angularities up to 75 degrees and successfully predict flow conditions with high accuracy.

The non-dimensional angle and pressure coefficients used internally in the data reduction algorithm have an almost negligible dependence on Reynolds number and a more pronounced dependence on Mach number. A test point at a certain Mach and Reynolds number can be reduced with calibration data taken at completely different Mach and Reynolds number and still predict the velocity vector, both magnitude and direction with reasonable accuracy. However reducing test data with a calibration file at the same Mach and Reynolds number will yield the most accurate predictions. Thus to obtain high prediction accuracy throughout the entire subsonic regime, it is necessary to calibrate the probe at a wide range of Mach and Reynolds number.



An uncertainty analysis of the 7-hole probe measurements was performed. Three procedures were followed to determine the uncertainty: a combined analytical and numerical analysis of how uncertainties in the pressure measurements propagate through the algorithm, uncertainty evaluation of the LLS surface fitting procedure and evaluation of the uncertainty of the algorithm using data verification test files. The results from the surface fit analysis showed that the contributing errors due to just the local least-squares surface fit are negligible. These uncertainties were on the order of  $10^{-5}$  degrees for angle calculations and  $10^{-3}$  percent for velocity magnitude calculations. Both the analysis of the error propagation through the algorithm and the uncertainty evaluation with test verification files gave similar results. Angles can be predicted to within 0.6 degrees with 99 % confidence and velocity magnitudes can be predicted to within 1.0 % also with 99 % confidence, while the corresponding uncertainties (standard deviation of the error distribution) are less than 0.2 degrees in angle prediction and less than 0.35% in velocity magnitude prediction.

## **ACKNOWLEDGEMENTS**

This work was supported by NASA Langley, Flow Modeling and Control Branch, Mr. William Sellers monitor, under grant NAG-1-1753, and by Aeroprobe Corporation, under project 32525-52050. The authors would like to greatly acknowledge the contribution of Mr. Richard Allen, whose machining dexterity made the fabrication of the miniature probes possible.

## **REFERENCES**

- 1 Kjelgaard, S.O., "Theoretical Derivation and Calibration Technique of a Hemispherical-Tipped, Five-Hole Probe," NASA Technical Memorandum 4047, 1988.
- 2 Bryer, D.W. and Pankhurst, R. C., "Pressure-Probe Methods for Determining Wind Speed and



Flow Direction,” Her Majesty’s Stationary Office / National Physics Laboratory, The Campfield Press, St. Albans, 1971.

- 3 Rediniotis, O. K., Hoang, N. T., and Telionis, D. P., “The Seven-Hole Probe: Its Calibration and Use,” Forum on Instructional Fluid Dynamics Experiments, Vol. 152, June 1993, pp. 21-26.
- 4 Zilliac, G.G., “Calibration of Seven-Hole Probes For Use in Fluid Flows With Large Angularity,” NASA Technical Memorandum 102200, December 1989.
- 5 Gerner, A. A. and Maurer, C. L., “Calibration of Seven-Hole Probes Suitable for High Angles in Subsonic Compressible Flows,” United States Air Force Academy-TR-81-4, 1981.
- 6 Everett, K. N., Gerner, A. A. and Durston, D. A., “Seven-Hole Cone Probes for High Angle Flow Measurements: Theory and Calibration,” AIAA Journal, Vol. 21, No. 7, July 1983, pp. 992-998.
- 7 Ames Research Staff, “Equations, Tables and Charts for Compressible Flow,” NACA Report 1135, 1953.
- 8 Krause, L. K. and Dudzinski, T. J., “Flow Direction Measurement with Fixed Position Probes in Subsonic Flow over a Range of Reynolds Number,” Proceedings for 15<sup>th</sup> International Aerospace Symposium, Las Vegas, Nevada, 1969, pp. 217-223.
- 9 Ainsworth, R. W., Allen, J. L. and Batt, J. J., “The Development of Fast Response Aerodynamic Probes for Flow Measurement in Turbomachinery,” Journal of Turbomachinery, Vol. 117, October 1995, pp. 625-634.
- 10 Dominy, R. G. and Hodson, H. P., “An Investigation of Factors Influencing the Calibration of Five-Hole Probes for Three Dimensional Flow Measurement,” Journal of Turbomachinery, Vol. 115, July 1993, pp.513-519.



- 11 Moffat, R. J., "Contributions to the Theory of Single-Sample Uncertainty Analysis," Transactions ASME Journal of Fluids Engineering, Vol. 104, June 1982, pp. 250-260.
- 12 Kline, S. J. and McClintock, F. A., "Describing Uncertainties in Single-Sample Experiments," ASME Mechanical Engineering, Vol. 75, Jan. 1953, pp. 3-8.

## **LIST OF TABLES**

Table 1. Calculated standard deviations using the "jitter" approach.

Table 2. Calculated standard deviations using a number of experimental test verification files.

## **LIST OF FIGURES**

Figure 1. Schematic of the 7-hole conical tip probes calibrated and tested (all dimensions in inches).

Figure 2. Probe Calibration Tunnel configuration for 7-hole probe calibration.

Figure 3. 7-Hole probe calibration envelope shows Mach and Reynolds number distribution in the calibration database for total pressures of 17, 32 and 60 psi.

Figure 4. Coordinate systems and flow angle definitions for the calibration of the 7-hole probes.

Figure 5. Sector arrangement and roll reference definition for a 7-hole probe.

Figure 6. A local least-squares interpolation surface with triangulation in the b1-b2 plane.

Figure 7. Schematic of the triangulation criterion in the b1-b2 plane.

Figure 8. Schematic of local distribution of calibration points around a test point in the neighborhood of the boundary between two sectors.

Figure 9. Dependence of coefficients b1 and b2 on Mach number.

Figure 10. Dependence of coefficients b1 and b2 on Reynolds number.

Figure 11. Dependence of coefficients  $A_t$  and  $A_s$  on Mach number.



Figure 12. Dependence of coefficients  $A_t$  and  $A_s$  on Reynolds number.

Figure 13. Distribution of the pressure measurement uncertainty over the range of calibration conditions.

Figure 14. Typical error histograms for: (a) pitch angle, (b) yaw angle, (c) cone angle, (d) roll angle and (e) velocity magnitude. Angle errors are in degrees and velocity magnitude errors are in percent.



Data	Standard deviation	Units
Pitch/Cone	0.1369	[deg]
Yaw/Roll	0.1972	[deg]
Velocity	0.3212	[%]

Table 1, Johansen et al.



Quantity	Standard deviation	Units
Pitch	0.0495	[deg]
Yaw	0.0547	[deg]
Cone	0.1465	[deg]
Roll	0.1855	[deg]
Velocity	0.3426	[%]

Table 2, Johansen et al.



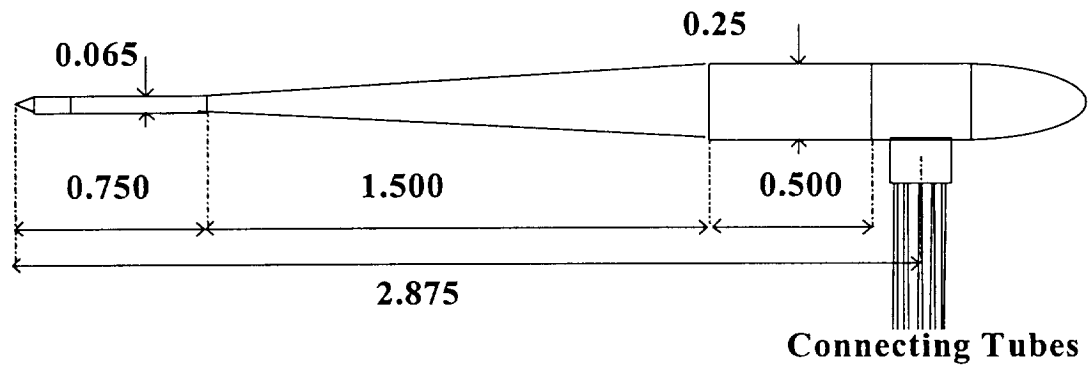


Figure 1, Johansen et al.



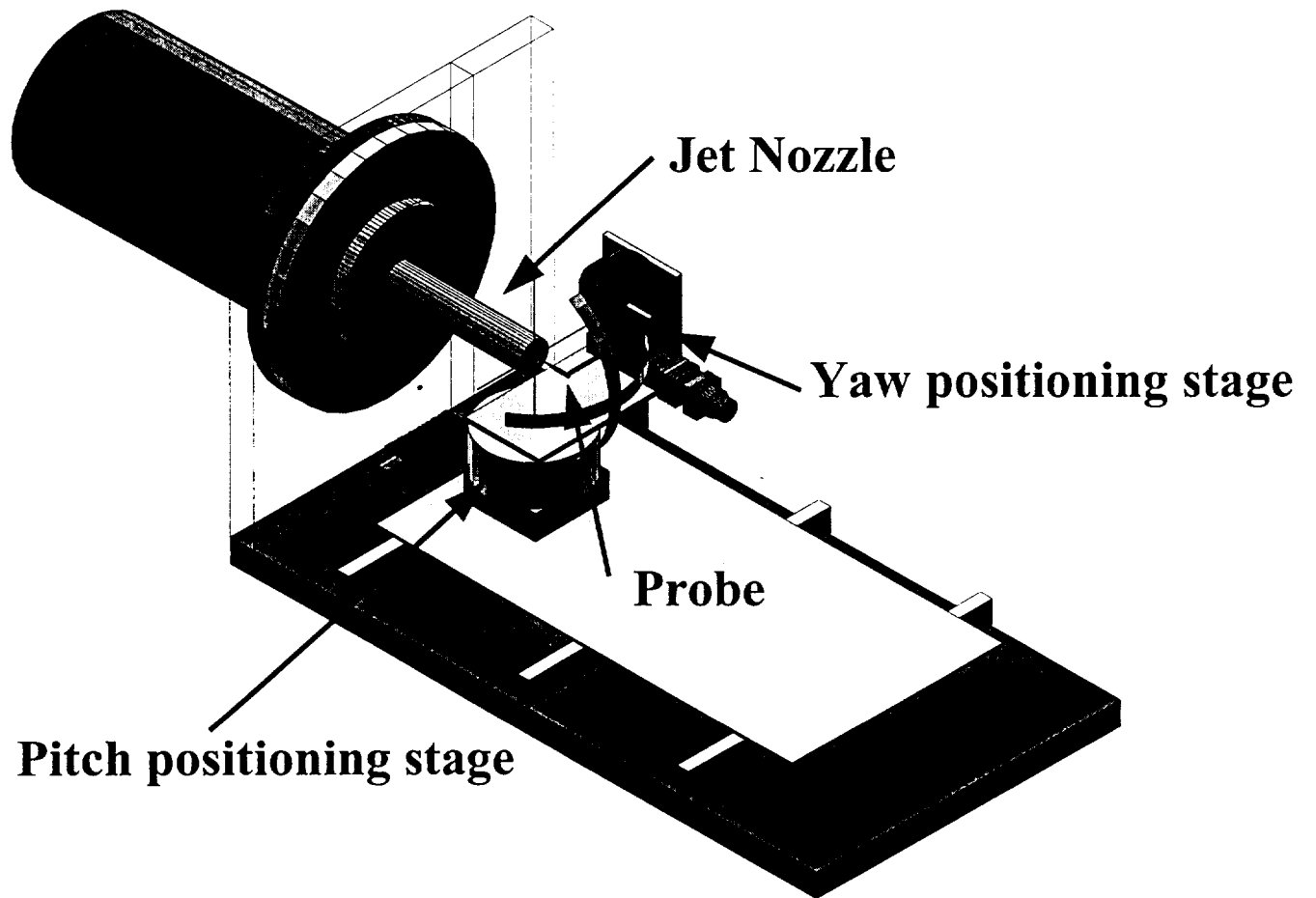


Figure 2, Johansen et al.



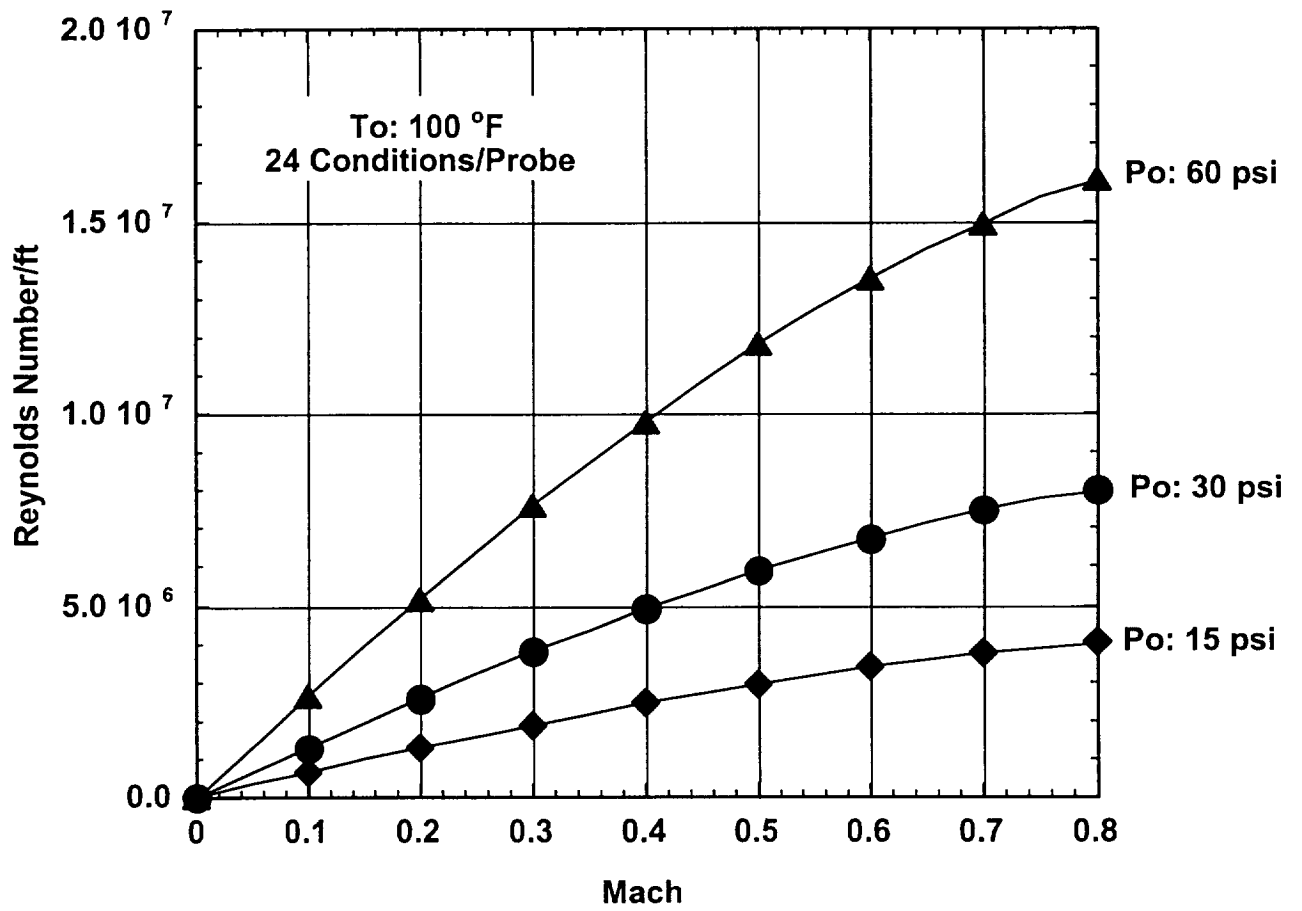


Figure 3, Johansen et al.



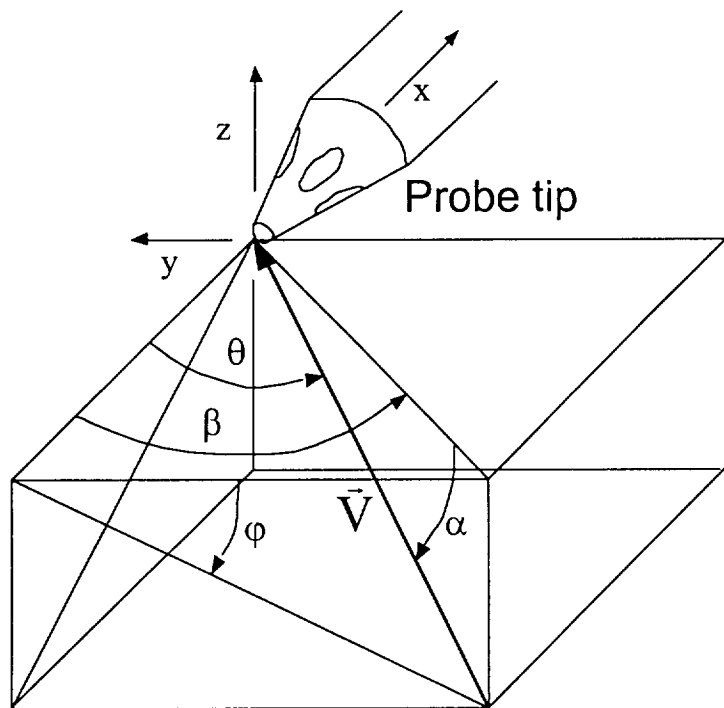


Figure 4, Johansen et al.



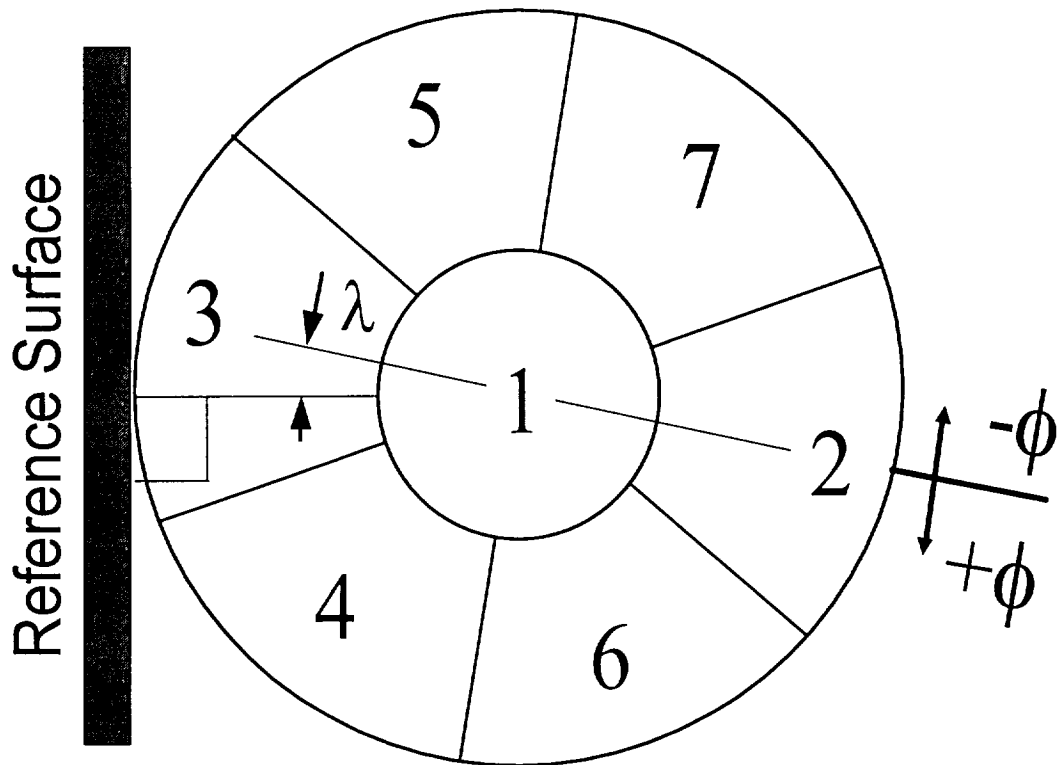


Figure 5, Johansen et al.



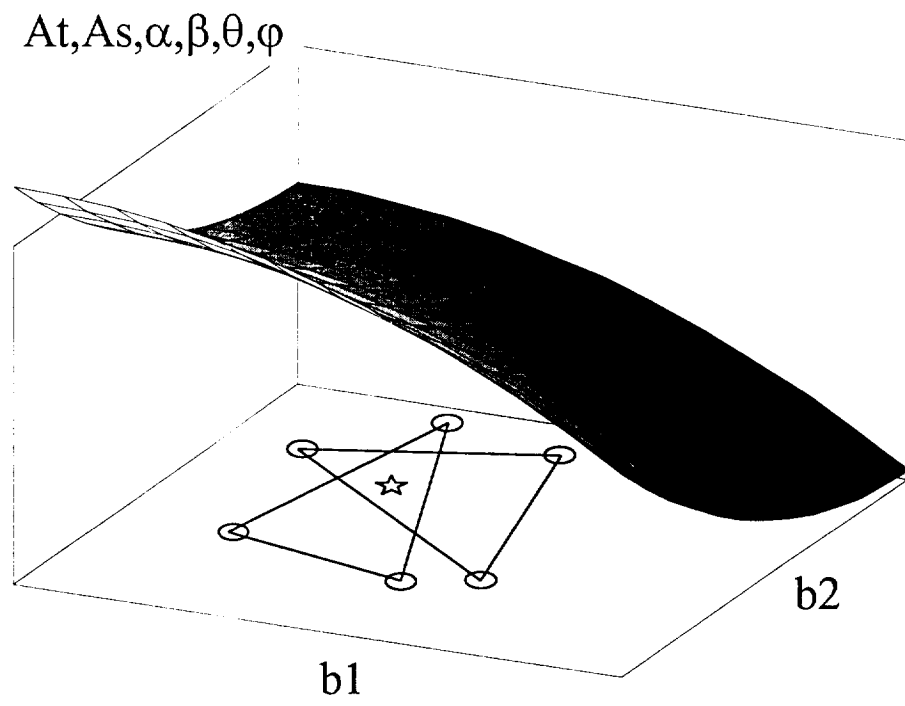


Figure 6, Johansen et al.



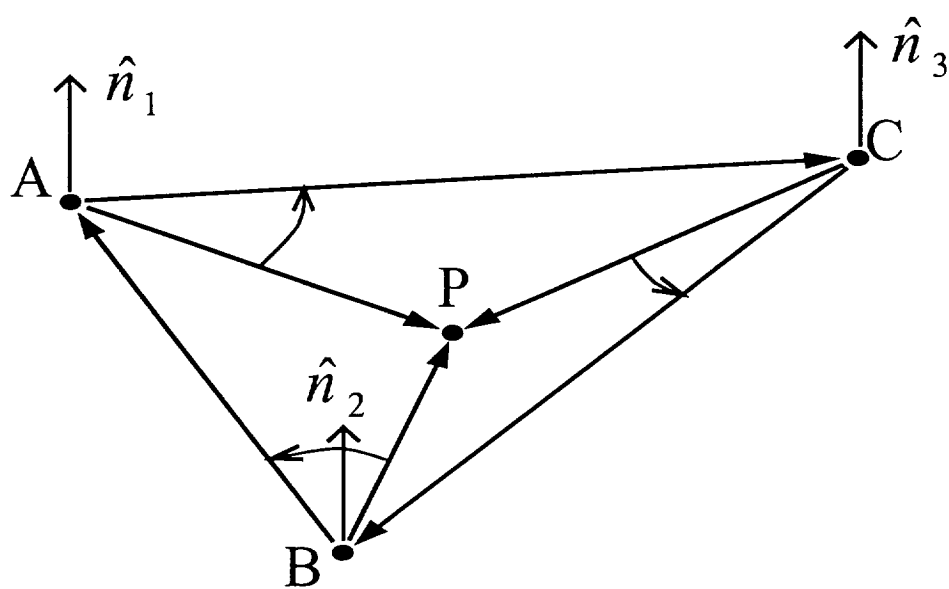


Figure 7, Johansen et al.



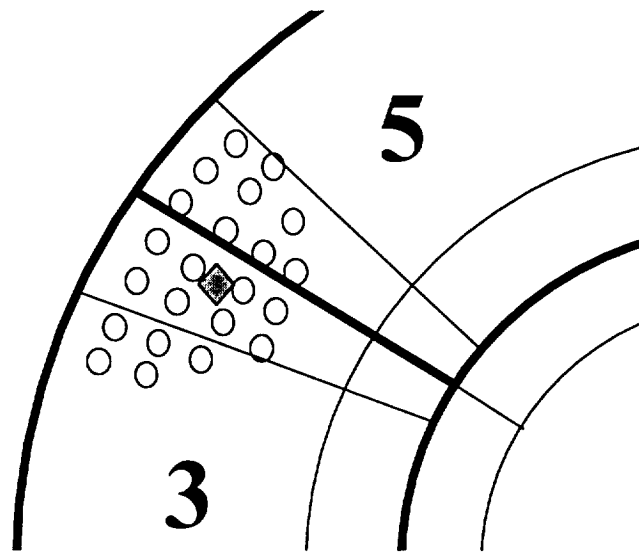


Figure 8, Johansen et al.



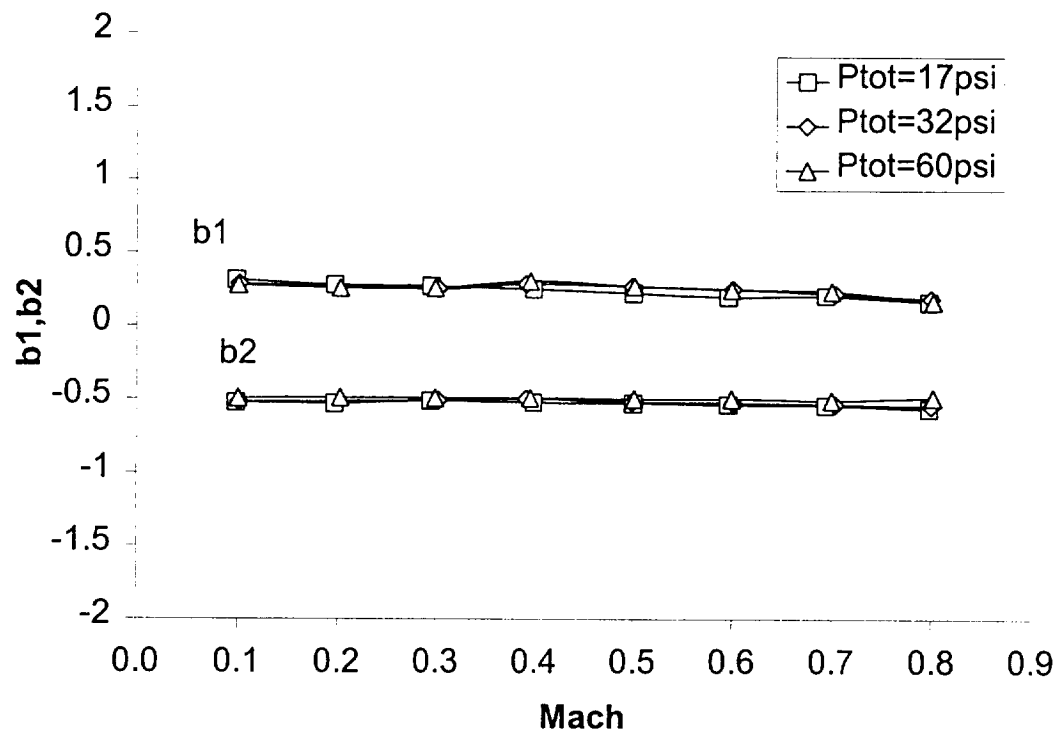


Figure 9, Johansen et al.



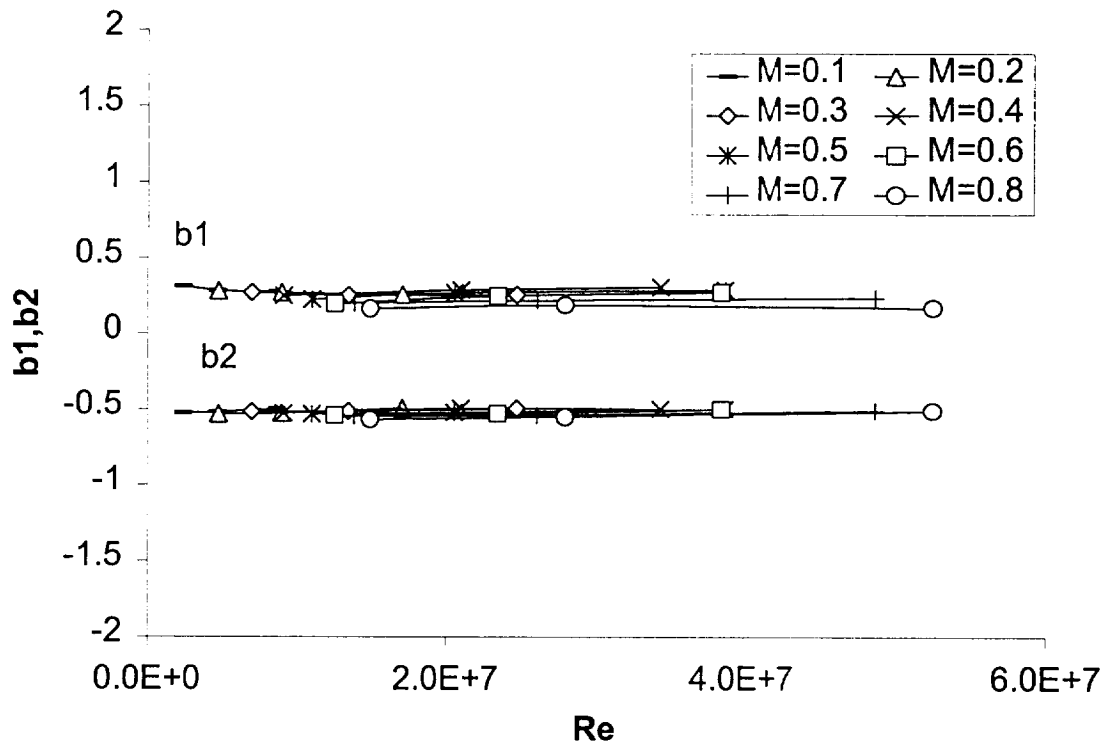


Figure 10, Johansen et al.



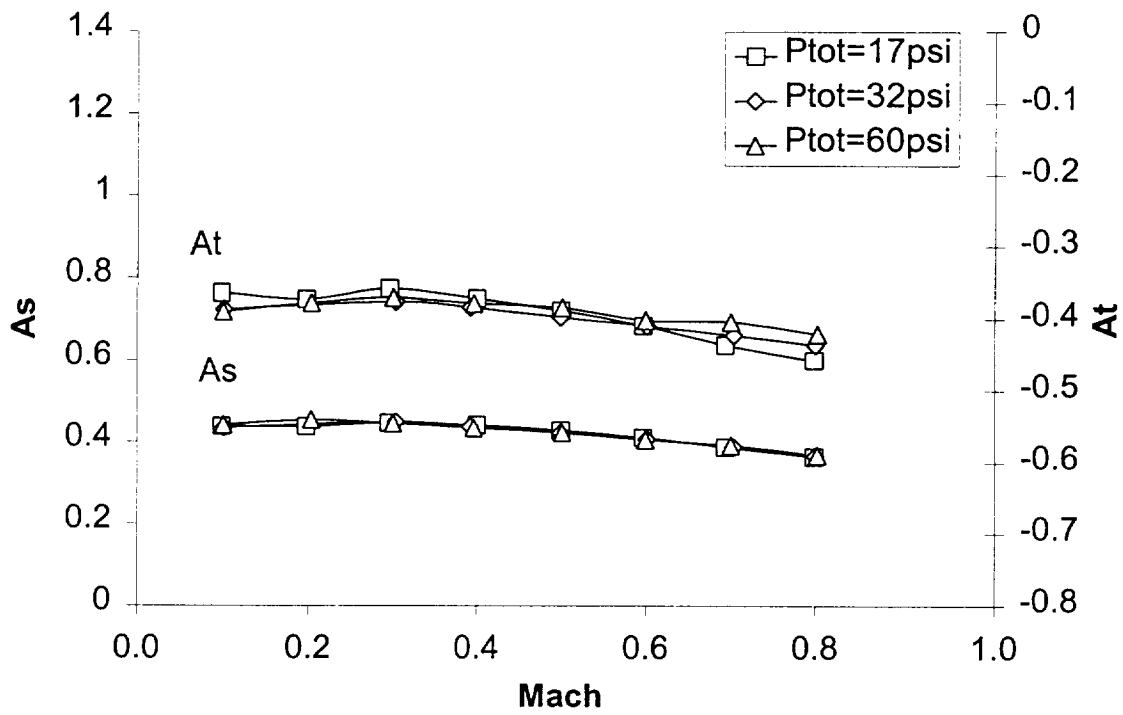


Figure 11, Johansen et al.



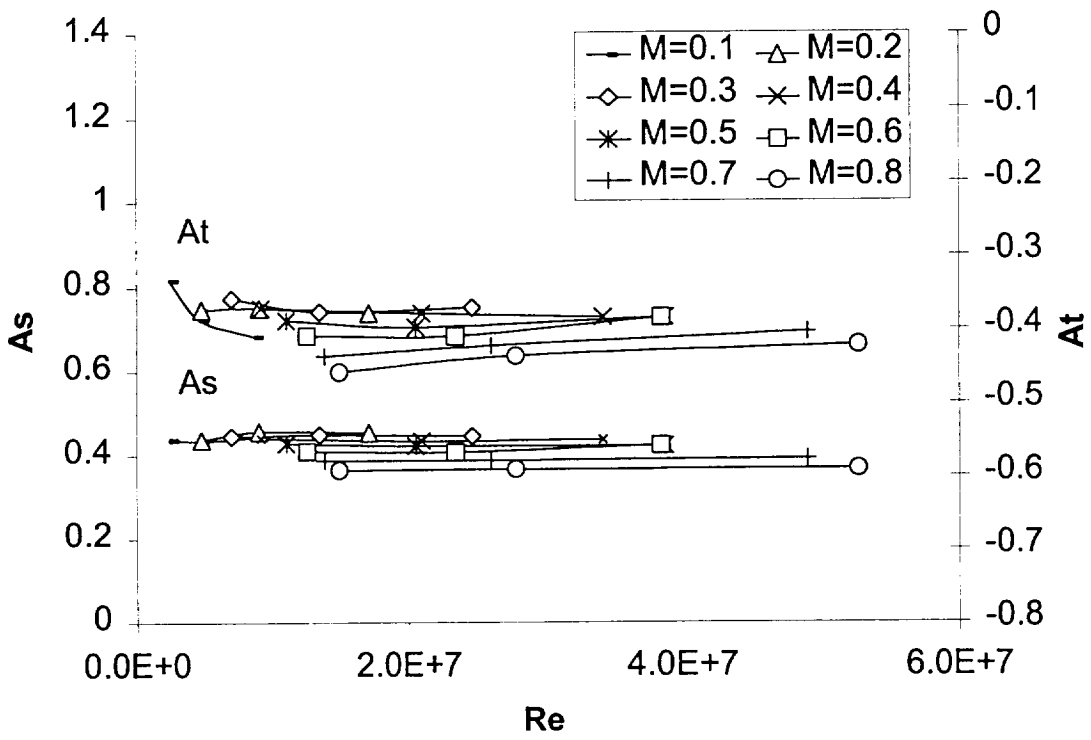


Figure 12, Johansen et al.



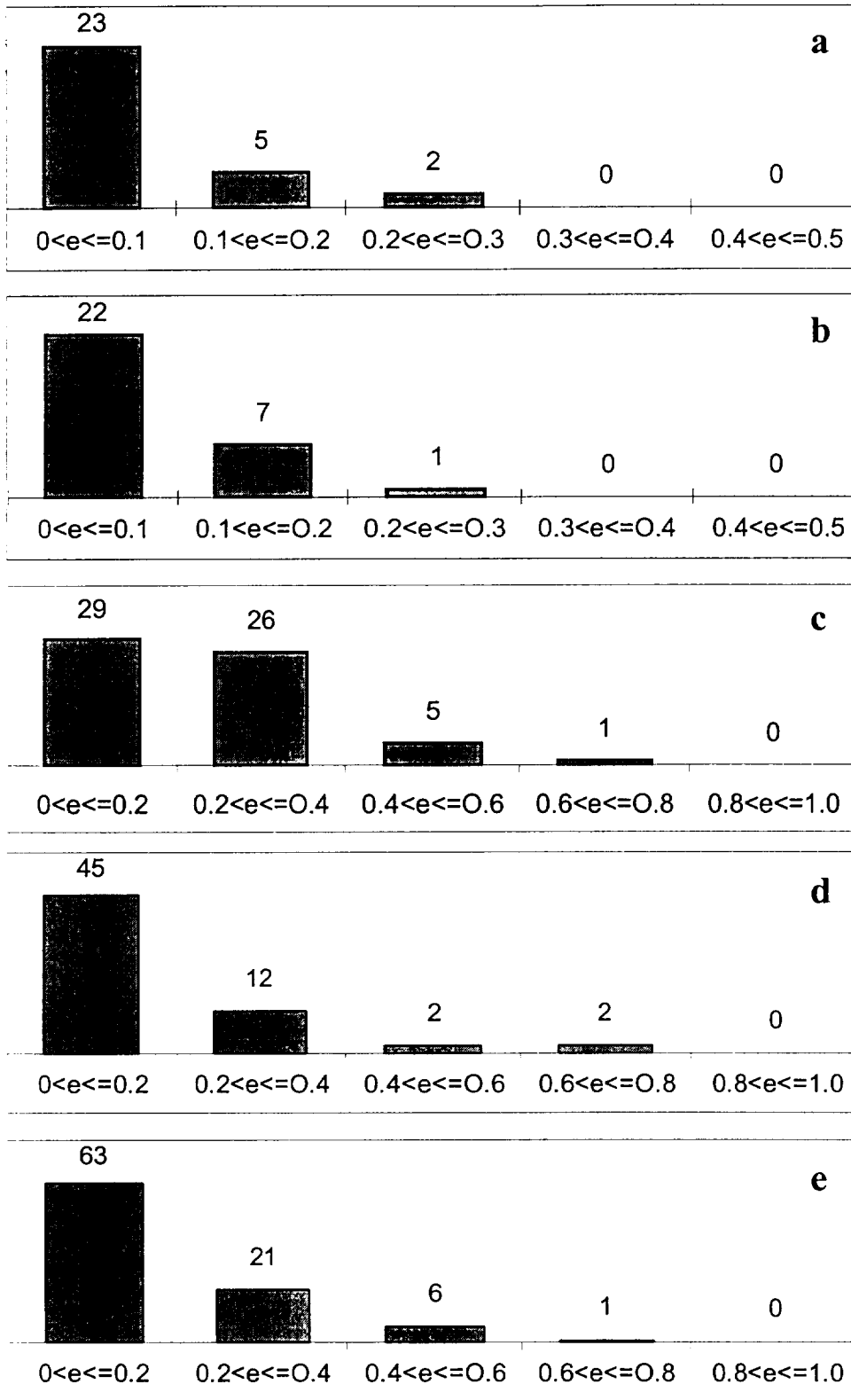


Figure 14, Johansen et al.



# **APPENDIX D**



## Introduction to PROBENET

This is a set of guidelines to familiarize the user with the features of PROBENET.

PROBENET is an extensive code tailored to deal with the calibration of 5 and 7 hole probes in incompressible and compressible flow environments. Although the user can design his/her own networks to optimize performance, he/she can also leave it to the code to select the optimal networks for the calibration. This will be explained in detail later.

PROBENET has been extended to include the calibration of probes in the compressible regime as well and the user is given an option in the main menu for calibrating the probe either in the incompressible regime or in the compressible regime. Based on whether the probe is calibrated in the incompressible or the compressible regime, there are two feedforward codes to predict the parameters like the pitch(or cone) , yaw(or roll) and the velocities from the test data file.

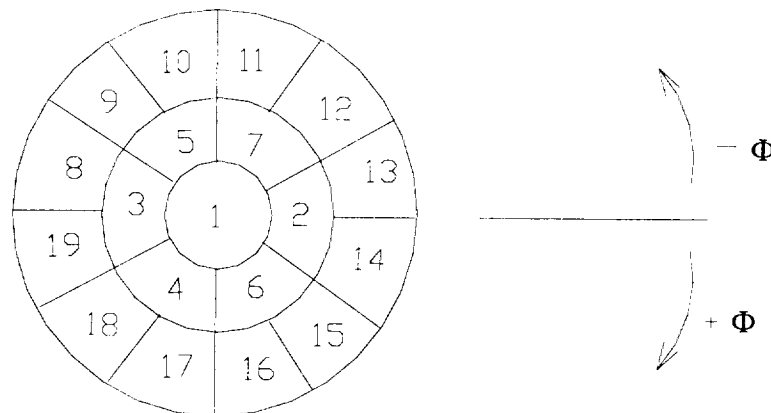


*Figure 5: The 7-hole domain split up to enhance neural network performance*

### ***Neural Network Training Algorithm***

The PROBENET training algorithm accepts as its input a raw pressure data file containing the calibration data for the probe. This data file is then converted to training vector files for every sector of the probe. To improve the efficiency and performance of the neural networks the high angle regimes of the probes were split up as shown in fig.5. This means that a 7 hole probe would have 19 sectors and a 5 hole probe would have 13. The training vector files are used to train the neural networks and an output binary file is then created which contains all the trained network information. This binary file is then used by the feedforward procedure to reduce any new pressure data acquired with the calibrated probe to the velocity components and the orientation angles.



One of the salient features of PROBENET is the range of available control over the network architecture. Typical commercial codes allow for an input layer, a few hidden layers (limited number) each one with a specific activation function for the entire layer, and an output layer with its activation function. But PROBENET allows the user to specify different activation functions at each node. The figure below (fig.6) shows a typical network structure which could be used to train and predict the pitch angle. The input layer accepts two element input. In the figure, f1 through f9 are the activation functions applied at each node. PROBENET currently uses several user-defined activation functions that are assigned to individual network nodes. These include constant, linear, quadratic, cubic, logsig, tansig, cosine, sine and exponential functions. These functions can be customized and new activation functions can be defined by the user.

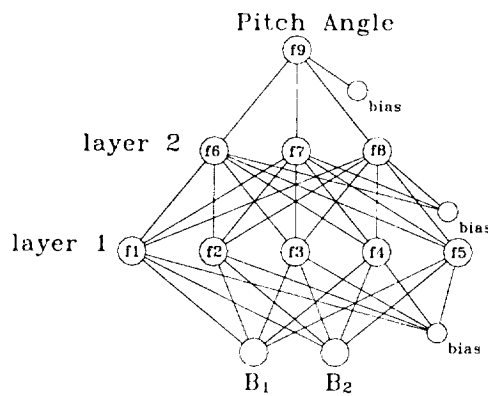


**Figure 6:** A typical network structure that takes a two element input to train and predict the pitch angle.

**Calibration data file format ( trnprb.dat on diskette) for a 7 hole probe in incompressible calibration :**

```

0.0000 -175.0500
1 13.5660
2 5.7900
3 6.1960
4 5.6980
5 6.0880
6 5.9430
7 5.7510
8 13.6060
0.0000 -171.4500
1 13.6290
2 5.8080
3 6.2200
4 5.7360
5 6.1030

```



6 5.9810  
7 5.7540  
8 13.6620

In the sample file shown each group of data includes 9 lines: Cone angle, roll angle (both in degrees) followed by the eight pressures (in torr) each labeled by an integer. The first seven pressures are from the ports of the probe while the eighth one is the tunnel dynamic pressure. All pressures are with respect to a tunnel reference pressure. The order of these pressures is important and should correspond to the port numbering of fig.2.

The same format has to be adopted for the data file with the test points. However, the freestream dynamic pressure is not necessary in the feedforward mode.

***Calibration data file format (2\_01\_cal.dat on diskette) for a 7 hole probe in compressible calibration:***

The input data file for a compressible formulation should contain data to be organized in the following order:

Probe number  
Mach number  
Reynolds number  
Total pressure (psi)  
Static pressure (psi)  
Total temperature (F)  
q compressible (psi)  
velocity (ft/s)  
density (lb-m/ft<sup>3</sup>)  
cone angle (deg.)  
roll angle (deg.)  
P<sub>1</sub>  
P<sub>2</sub>  
P<sub>3</sub>  
P<sub>4</sub> (P<sub>1</sub> through P<sub>7</sub> in psi)  
P<sub>5</sub>  
P<sub>6</sub>  
P<sub>7</sub>

P<sub>1</sub> through P<sub>7</sub> correspond to the seven pressures from the seven ports. Again the order in which the pressures are recorded is important and is depicted in fig.2. This format of the file can be easily generated by using the preprocessor program described in section .....

As already mentioned, to enhance the performance of the neural networks, the six peripheral ports (fig. 2) were split up as shown in fig.5 for training purposes alone. It should be noted from fig.5, for example, that subsectors 2,13,14, correspond to the original sector 2 (fig.2), while subsectors 3,8,19 correspond to the original sector 3, and so on. For the purposes of the present discussion the subsectors numbered 2 through 7 will be referred to as high-low sectors and those numbered 8 through 19 will be referred to as the high-high sectors.



## *Training Procedure*

When the user executes the command PROBENET.EXE at the dos prompt, the following menu is displayed:

```
---PROBENET NEURAL NETWORK CALIBRATION PROGRAM---  
***** Multi- Hole Probe Calibration *****
```

```
EXIT: Exit program  
MAKE: Make Vector file from pressure data  
OPEN: Open an existing vector file  
START: Start calibration algorithm  
INFO: Display program information  
OPTN: Options menu  
SNET: Single network training program
```

*PROBENET->*

To start off with the calibration, the first thing that needs to be done is to convert the raw data calibration files to a form that would be used by the neural networks for training purposes. Therefore the user has to generate what are called the training vector files from the input data file. To do this the “MAKE” option should be selected. This option prompts the user to enter the name of the data file that is to be used for calibration and a name for the training vector files as well.

When all the information has been entered the training vector files are generated for all the nineteen sectors of the probe. A typical training vector file generated has the following format:

14	.51499	-.21895	-.06704	.63609	32.00000	-4.77060
14	.50717	-.51558	-.06319	.64118	32.02710	-8.76660
14	.47563	2.33399	-.44271	.50513	32.98500	25.90520
14	.51408	1.95100	-.31931	.54406	32.84451	22.25660
14	.54029	1.59981	-.22315	.57919	32.68000	18.56950

The first field in the training vector file record denotes the sector having the maximum pressure. Sector 14 corresponds to port 2 (fig.5). The two real numbers that follow are the two pressure coefficients that are the inputs to the neural network. The last four values are the parameters that are used to train the neural networks namely,  $A_t$ ,  $A_s$ ,  $\theta$  (or  $\alpha$ ),  $\phi$  (or  $\beta$ ) respectively. When “MAKE” is selected and the training vector files are generated the extensions for the training vector files are automatically set to .cfA through .cfS, where the letters A through S are indicative of the sectors 1 through 19.

The “OPEN” procedure opens a specific training vector file that has already been created using the “MAKE” procedure.

The “START” option initiates the training of the neural networks with the training data contained in the training vector files generated. When “START” is selected the user is asked to select a probe type (5 hole or 7 hole) and the user is asked to make a selection:



*You may choose to initialize the network structure and the weights with either:*

- (1) the optimal network database*
- (2) a previously trained Network Information file*

The design of a neural network structure that is optimal for a certain system is time consuming and tedious. The number of hidden layers, the type of activation function, etc. are some parameters that the user has to vary in the process of optimizing a network structure. PROBENET has built within itself a set of such networks to spare the user from the lengthy optimization process. For this the user should select option (1) from above. PROBENET then initiates an optimization procedure that does not require the intervention of the user. The code trains the networks with the calibration data that is provided, compares their relative performance and decides on which network is optimal for the probe. It then creates a binary output file - the network information file - with the details of the trained networks. This file serves two purposes:

- a) it is the input to the feedforward subroutine
- b) it can be used to further train a network when option (2) is selected from above.

When option (2) is selected the user will be asked to enter the filename (without the extension) of the particular Network Information file that was generated while using option (1). When this option is selected the code does not perform any optimization but merely trains the networks described in the Network Information file.

When option (1) or (2) is selected the user will also have to

- a) Enter the filename (without the extension) of the output Network Information file.
- b) Specify the convergence value in terms of the target absolute mean error.

The training will be terminated if:

- a) the maximum number of training cycles is reached or,
- b) the absolute mean error drops below the targeted one.

It has been seen from experience that the maximum number of training cycles when option (1) is selected should be between 400 and 500 for better results. In this first phase of training, the larger the maximum number of cycles the lesser the necessity to refine the surfaces that do not perform well (will be explained in detail later). If the time required to calibrate the probe is not of great concern then it is recommended that the maximum number of cycles be around 2000 or even greater. When option (2) is selected the maximum training cycles to converge to the target mean error is decided by the code. The suggested value for CONVERGENCE for option (1) is in the range 0 to 0.3.

When "OPTN" is selected the user can specify all the parameters to be used in the training process. Learning rate, momentum, increment, decay, buffer margins, etc. are some of them. Every time the user has to specify such values, the code guides him/her by indicating a range of typical values for that particular parameter.

The user can design his/her own network by selecting the "SNET" option of the menu. This will place the user in an individual network training environment. Suppose the user does not leave the optimization process to PROBENET or that the user finds some surface in some sector has not been trained well, then this option helps the user to design and test his/her own network or refine a bad surface. It should be mentioned here that the Network Information file contains information about all the 76 networks: 19 sectors (7 hole probe, fig.5) with each sector being associated with 4 networks corresponding to the flow variables  $A_t$ ,  $A_s$ ,  $\theta$  (or  $\alpha$ ),



$\phi$  (or  $\beta$ ). The user can replace any of these 76 networks. In doing so, the user has to first design the network. This is done in the form of Initialization files (with extension .IN). A sample Initialization file is given below to illustrate its structure:

#### Network Initialization file

```
sector    = 1

surface   = 1    (1 refers to the variable At)

maxcycles = 2000

convergence = 0.00

num_layers = 4    ( 1 input layer, 2 hidden layers and 1 output layer)

num_nodes(1) = 2    ( input layer)

num_nodes(2) = 4    ( 1st hidden layer)

num_nodes(3) = 4    (2nd hidden layer)

num_nodes(4) = 1    (output layer)

Activ Func(2)= 9 9 9 9 ( 9 refers to the log-sig activation function)

Activ Func(3)= 1 1 1 1 ( 1 refers to the linear activation function)

Activ Func(4)= 1

learning rate= .01

LR momentum = .95

LR increment = 1.05

LR decrement = 0.7

LR threshold = 1.05
```

Activation functions must be listed on same line with 2 spaces between integer values. LR refers to the learning rate the theory of which has been explained in the *Artificial learning* section. (It is advised to the user that the same learning rate parameters be retained for any new structure defined by the user.)

The contents of these files are fairly self explanatory. The specific network has 4 layers with layer 1 being the input layer and layer 4 being the output layer. PROBENET



currently supports 9 activation functions and each of these is identified by an integer from 1 through 9. A list of the available activation functions and their corresponding integers is provided under the option "ACTV" of the "OPTN" menu. The various activation functions built within PROBENET are:

- 1 Linear activation function
- 2 Quadratic activation function
- 3 Cubic activation function
- 4 Tan-sig activation function
- 5 Sine activation function
- 6 Cosine activation function
- 7 User-definable activation function
- 8 User-definable activation function
- 9 Log-sig activation function

When the user has created his/her network structure and wants to test it, he/she must choose the "INIT" option from the "SNET" menu and then choose the "TRAIN" option. The code will then ask the user for other information namely, the filename, surface to be trained, etc. The surfaces  $A_t$ ,  $A_s$ ,  $\theta$  (or  $\alpha$ ),  $\phi$  (or  $\beta$ ) are referred to as 1 through 4. The mean error displayed during the training process gives a good picture as to the performance of the network. If the user is satisfied with his/her design i.e., if the defined network when trained and used for prediction gives errors within the allowable range, then he/she can choose the "NETIO" option and "LOAD", "WB" options to write the new network information in the Network Information file. The same process needs to be followed for refining a network for any surface that has not been trained well which will be explained in detail later.

It is possible to train the probe for multiple Mach numbers by filestreaming. The user should enter all the relevant data that is to be input to the code into a single file (say, RUN) in different rows and then type the command PROBENET<RUN at the dos prompt. This will start the training process and completely train for all the calibration files generating corresponding Network Information files without the user intervention.

### ***Single-file feedforward procedure***

Once the training is completed, it is necessary to validate the training to check if the trained networks yield good prediction accuracy. So, once the Network Information file has been generated for a particular test file, it can be used in the feedforward mode to predict the flow variables from pressure data acquired with the calibrated probe. However, this procedure can also be used for prediction in the real environment.

The feedforward code for incompressible formulation can be executed by entering *PROBEINC.EXE* at the DOS prompt while the feedforward procedure for the compressible formulation can be executed by entering *PROBECOMP.EXE*. The format for the test file used for predicting results in the real environment is as described:

For the incompressible formulation, the test file should have the seven pressures (in torr) in a column format with one line space between each set of data if prediction is to be done in a real environment. For validation purposes, the test file can have the same format as the calibration file.



1	13.5660
2	5.7900
3	6.1960
4	5.6980
5	6.0880
6	5.9430
7	5.7510

1	13.6290
2	5.8080
3	6.2200
4	5.7360
5	6.1030
6	5.9810
7	5.7540

For the compressible formulation, the test file should have:

the probe number, the reference pressure (in psi), the total temperature (in degrees F) and the seven measured pressures (in psi, relative to the reference pressure) in the same order in a single row. Again, for validation purpose, the test file should have the same format as the calibration file as described earlier.

Validation is done to check if the networks have been trained well. In this case the error between the actual values and the predicted values will be written to the output file as well. However, if these procedures are used for prediction in a real environment, the predicted values alone are written into the output file. In the validation mode, the output file that is generated contains the following data:

test point number, predicted  $u$ ,  $v$ ,  $w$  components of velocity (in ft/s), actual velocity magnitude (in ft/s), predicted velocity magnitude (in ft/s), velocity magnitude error (in ft/s),  $A_t$ , predicted  $A_t$ ,  $A_s$ , predicted  $A_s$ , actual pitch/cone angle (in deg.), predicted pitch/cone angle (in deg.), pitch/cone angle error (in deg.), actual yaw/roll angle (in deg.), predicted yaw/roll angle (in deg.), yaw/roll angle error (in deg.), actual Mach number, predicted Mach number ( these two fields are generated only for the compressible formulation case), port number to which the test point corresponds and finally the subsector to which it corresponds as per our definition of the sectors (fig.5).

This is useful for refinement purposes as explained later. The algorithm used for the feedforward procedure is explained in a later section.

### ***Calibration File Refinement***

During the first phase of training when the optimal neural network is being selected, we train each network typically for 400-500 cycles. The code picks the network that performs well in these 500 cycles as the optimal network. It has been seen from experience that some networks that perform well for the first 500 cycles do not train very well in the second phase of training where the optimal network is trained further. On the other hand, networks that do not train very well in the first 500 cycles might do well in the second phase of training. For this reason, it sometimes becomes necessary to track the bad network manually and refine it.



To eliminate this manual refinement it is advised that the user train the networks in the first phase for 2000-3000 cycles in which case the user would have to compromise on the time taken for training. Typically, if a low number of training cycles (about 500) is selected in the first phase of training it is seen that out of a test file that contains around 1500 test points, the user might have to manually refine the surface  $A_s$  for 2 to 3 subsectors.

The code in the Validation mode allows the user to check if the already trained networks perform well by generating the error values for the predicted data. In the output file generated in the feedforward mode the user can identify those sectors or surfaces that have large errors. These surfaces call for refinements which could be performed as described below:

The user should make note of the sector and the surface(  $A_t$ ,  $A_s$ , pitch/cone or yaw/roll) whose predictions have errors more than the permissible limit. Then the user must select the 'SNET' option from the main menu. This option displays another menu:

```
---PROBENET NEURAL NETWORK CALIBRATION PROGRAM---  
***** Single Network Training *****
```

```
EXIT  : Exit program  
MAKE  : Make vector file from pressure data  
INIT  : Initialize network structure  
NETIO : Read and write network information data  
VIEW  : Display network to screen  
TRAIN : Train new network  
RETRN: Retrain an existing network  
RUN   : Run trained network in feedforward mode  
INFO  : Display program information  
OPTN  : Options
```

Next the user must select 'OPTN' to enter the probe type (5 hole or 7 hole probe) and number of sectors (19 for a 7 hole probe or 13 for a 5 hole probe). Then the user must select the 'INIT' option. Under this option the user needs to specify the network architecture that he/she is going to try for a particular surface. It is strongly advised to the user that the network architectures used for refining surfaces be selected from the existing database of network structures named as bpb0001.in through bpb0020.in. After entering the filename that contains the network architecture, the user must select the 'TRAIN' option from the above menu. This option further calls another menu on the screen:

```
---PROBENET NEURAL NETWORK CALIBRATION PROGRAM---  
***** Training menu *****
```

```
..      : Back up to previous menu  
EXIT   : Exit program  
RAND   : Create random initial weights  
SPIKE  : Perturb existing weights  
VIEW   : Display weights to screen  
START  : Train new network
```



From this menu the user should select the 'RAND' option followed by the 'START' option. This is to randomize the initial weight vectors. Then the user will be asked to specify the vector file used for calibration, number of cycles and other relevant information. It is advised that a maximum of 4500 or 5000 cycles be used for calibration.

Once the network has calibrated the surface it is time for testing the calibrated surface. So the user now has to back up two menus by using the '.' option and select the 'RUN' option from the menu displayed. The code will again guide the user to input relevant information and generate an output file with the actual values for that surface being trained, predicted values and the error between the two. If the error is acceptable, the user needs to select the 'NETIO' option and then 'LOAD' followed by the 'WB' options to write the information for this particular network in the Network Information file. This way refinement of surfaces is accomplished. However, it is seen that on an average the code's judgement regarding the optimal network structure for a particular surface is fine. Generally, it has been seen that the angle predictions are fine but the velocity predictions may sometimes give large errors. Under such circumstances the user may have to refine the networks for the corresponding  $A_s$  to get better predictions for velocity. Again, manual refinement can be eliminated if the user selects the number of training cycles around 2000-3000 in the first phase of training.

### ***Multi-file feedforward scheme***

The multi-file prediction scheme is a 2-D interpolation scheme based on the Reynold's number and the Mach number. Typically, when a probe is trained, the naming convention used for the Network Information file generated by the code is as follows: tm3\_03.bin where, the digit 3 stands for the probe number, and 03 stands for the Mach number for which the probe has been trained ( $M=0.3$ ). The extension is automatically generated by the code. When a probe has been trained for all the Mach numbers, for example, 0.1 through 0.8, we have a set of Network Information Files for the probe. It should be borne in mind that if the probe were calibrated in higher Mach number flows close to the transonic regime the results would not be accurate.

The prediction scheme enables the user to put the pressure data corresponding to different Mach numbers in a test data file and perform the data reduction for different Mach numbers at a time. For this it should be ensured that the Network Information files corresponding to all the Mach numbers have already been generated or in other words the probe has already been calibrated for all Mach numbers. To use the prediction scheme, the user has to first generate the lookup file which can be done by simply typing LOOKUP at the dos prompt which will generate the lookup file containing the training file name, the Reynold's number and the Mach number corresponding to that training file. Once this is done the user should simply type *FEEDFORW.EXE* at the dos prompt. The code will guide the user regarding the information that needs to be input. The test files should have the same format as described under the Single-file feedforward scheme.



# **APPENDIX E**



# **MULTIPROBE**

**Version  
AeroProbe™ Beta (3.0)**

## **USER MANUAL**

Version

**JULY 21, 1999**

Last Updated

**JULY 29, 1999**



## **INTRODUCTION**

*MultiProbe is a data reduction program for 5- or 7-hole pressure probes. The program is versatile in the sense that it accepts almost any data format, units, probe type and configuration and flow type. The program can successfully reduce data from probes in any subsonic flow and predict the flow velocity vector, both direction and magnitude with a high degree of accuracy.*

## **DESCRIPTION OF THE PROGRAM**

MultiProbe uses at least one calibration file (raw data file) and converts that data file to new (binary) data file that can be used to reduce probe data from unknown flow fields. There are a number of input variables that must be entered into MultiProbe to ensure correct data reduction. To simplify the reduction all of these values are stored in a probe database. The probe database should also be given a name. When preprocessing the raw calibration data files, the user must go through several steps to explain the units and format of the raw data. The raw data file is then converted to the MultiProbe internal format (metric units) and a binary file is created. The user is asked to give the binary file a name. Note: this file is the calibration file to use later when data reduction is performed. It is advised to store the probe profile database also, the user will be prompted if he wants to save the profile. Thus there is a minimum of four data files the user will encounter:

1. Raw calibration data file (\*.???)
2. One preprocessed calibration data file (\*.mpr)
3. Probe profile (\*.MPP)
4. Raw pressure data from probe in unknown flowfield (\*.???)

Saving the probe profile will later enable the user to open it and reduce data without re-preprocessing data or configuring the program. The probe profile contains all the information about the files, formats and units in the reduction. It also holds the name of the preprocessed calibration file, so that the user does not have to enter the calibration file to use when reducing data. MultiProbe 30 is currently only capable of holding one calibration file per profile, but will be later extended to hold multiple files and reduce a given test file with one or more of the files in the profile.

The methodology of reducing probe data is:

1. Preprocess the raw calibration data. See *Preprocessing Calibration Data*.
2. Optionally save the probe profile.
3. Reduce test data. See *Reducing Test Data from Unknown Flow Using A Calibrated Probe*.
4. Optionally graph the results. See *Analyzing Reduced Data*.

There are several other options available in MultiProbe they will be described in detail in this manual.



## ***PREPROCESSING CALIBRATION DATA***

Use **Data | Preprocess | Wizard** on the main menu.

### **Step 1. Calibration data files.**

Select one (1) calibration file for a probe. There will be an option in a later version to select multiple files.

(Note: Make sure that all of the calibration files have the same format if multiple files are preprocessed simultaneously. If they have different formats preprocess them one-by-one.)

### **Step 2. Data file format.**

Select either:

1. Aeroprobe format:

This format is:

Number of points Lambda

(Ttot XXX)\*

\*Only for certain files

Cone Roll

1 P1

2 P2

3 P3

4 P4

5 P5

6 Ptot\*

\*For 7-hole probe there are 7 pressures and Ptot is in #8

Cone Roll

1 P1

:

2. Data in columns (generic)

Select any type of data in columns where each row of data correspond to a set calibration point with discrete angles

### **Step 3. Probe type and calibration orientation.**

1. Select 5- or 7-hole probe.
2. Probe type: Conventional is only available. Fast response might be implemented later.
3. Probe shape. Determine the shape of the probe, either:
  - 3.1. Straight probe.
  - 3.2. "L" -shaped or "Elbow" probe.
  - 3.3. "C" -shaped or "Cobra" probe.
4. Probe tip shape.
  - 4.1. Conical.
  - 4.2. Hemispherical.
5. Calibration angle system.
  - 5.1. Cone/Roll system (typical for straight probes).
  - 5.2. Pitch/Yaw system (typical for L or C-shaped probes).



6. Select the probe port numbering, looking into the probe tip. Note the angle convention and the reference surface (for straight probes) or stem location (for L or C-shaped probes).
7. Enter a name or comment on the probe. (For the reference of the user).

#### **Step 4. Reference pressure.**

Reference pressure. Note: This pressure can be omitted if the static pressure, the port pressures and the total pressure in the calibration files are absolute or with respect to the static pressure (granted the static pressure is absolute).

- 1.1. Enter the reference pressure manually. Enter the reference pressure for differential pressure transducers. This pressure is in many cases the atmospheric pressure.
- 1.2. The reference pressure is provided in the calibration file. Select the column in the calibration files where the reference pressure can be found.
- 1.3. Type of pressure in points 1.1. or 1.2. this pressure must be absolute.
- 1.4. Units of the pressure in points 1.1. or 1.2. select from the list of pressures.

#### **Step 5. Static- and total pressures.**

1. Static pressure.
  - 1.1. Enter the static pressure manually.
  - 1.2. The static pressure is provided in the calibration file. Select the column in the calibration files where the static pressure can be found.
  - 1.3. Type of pressure in points 1.1. or 1.2. this pressure can be either absolute or relative to the reference pressure in step 4 point 1.
  - 1.4. Units of the pressure in points 1.1. or 1.2. select from the list of pressures.
2. Total pressure.
  - 2.1. Enter the total pressure manually. This pressure is in many cases the static pressure far upstream of the calibration point. (Use Bernoulli to correct if velocity is not zero upstream).
  - 2.2. The total pressure is provided in the calibration file. Select the column in the calibration files where the total pressure can be found.
  - 2.3. Type of pressure in points 2.1. or 2.2. this pressure can be either absolute or relative to the reference pressure in step 4 point 1 or relative to the static pressure in step 4 point 1.
  - 2.4. Units of the pressure in points 2.1. or 2.2. select from the list of pressures.

#### **Step 6. Port pressures.**

1. Select type of pressure.
  - 1.1. Differential with respect to the reference pressure in step 4 point 1.
  - 1.2. Differential with respect to the static pressure in step 5 point 1.
  - 1.3. Absolute.
  - 1.4. Pressures are voltages.
    - 1.4.1. Press blue arrow to define the slope and offset for pressure transducer in each of the ports.
2. Enter which column in the calibration file that the port pressures can be found.
3. Select the units of the port pressures. Note this has to be select also if you are using voltage inputs. (point 1.4.1.) where the units of the conversion must be entered.



**Step 7. Flow Temperature.**

1. Select total or static temperature provided.
2. Enter the flow temperature manually.
3. The flow temperature is provided in the calibration file. Select the column in which the temperature can be found.
4. Select the units of the temperature from list.

**Step 8. Angles.**

1. Select which column in the calibration file the angles can be found.
2. Select the type of angles used. Cone/ Roll system. Will be expanded later.

**Step 9. Calibration file format.**

1. Enter any number of test points attached at the end of the calibration file.
2. Enter any number of lines of headers, data description number of points etc. Count all lines of information (count also blank lines) before the actual numbers start.

**Step 10. Check of user entered information.**

1. Check if the information entered is correct by scrolling through the form.
2. If information is incorrect, go back to the particular form and change.

**Step 11. Calibration file analysis. (Form 9).**

1. Check if the information provided in the scroll screen is ok.
2. Check if any warnings have been issued. If there are any significant warnings redo the calibration or check the steps 1 through 10.

**Step 12. Save the preprocessed calibration file.**

1. Enter a file name for the preprocessed calibration file. A default extension \*.mpr is recommended (you do not need to enter this extension).

\*\*\* End of preprocessing the calibration file(s) \*\*\*

***QUALITY OF THE CALIBRATION***

The quality of the calibration and the data reduction algorithm can be checked using data verification points. This can only be done if a number of data points was recorded at the end of the calibration (a common practice) and if the points were identified in the preprocessing of the calibration file. See step 9 point 1.

***Data | Calibration Test |***

1. Select the surface fit type wanted. Currently only LLS is available.
2. Scroll through the screen to see if the reduction parameters are as desired (default values are typically sufficient for most applications).



3. Change any of the reduction parameters by pressing **Change** and changing the parameters on the specifications menu.
4. On **Proceed** a new window will appear. The data verification will start automatically. Please wait for the data reduction to complete. Once the reduction is complete the angle errors, velocity errors and the total and static pressures can be viewed. There is no need to press **Reduce** since the reduction has already been performed.
5. For the angle errors and the velocity errors the minimum, maximum, mean and standard deviation of the difference between the exact (as given in the calibration file) and the predicted (by the algorithm) values.
6. Close the screen to return to the main program.

Reducing test data from an unknown flowfield using a calibrated probe

### *Data | Reduce Data |*

MultiProbe can only accept data formats in columns, that is each row of data consists of multiple columns with all the necessary information and each row corresponds to one unique test point.

1. **File Format:** Enter number of file headers in the data file.
2. **Reference Pressure:** Enter the type and location of the reference pressure.
3. **Port Pressures:** Enter the type and location of the port pressures.
4. **Temperature:** Enter the type and location of the temperature.
5. **Proceed.** Give a filename for the data reduction results.
6. Wait for data reduction to complete.
7. The reduction results can be found in the file from step 5.

### *OPTIONS IN THE OUTPUT FILE*

#### **Specifications | Output File Format**

MultiProbe features a customizable output data file format. The data and the units to be included in the output file during data reduction is set here. The default mode is including all values with metric units. A header will be included in the output file which describes the content in each column and the units used. Following this the data will be in columns where each row corresponds a specific data point. It is to be noted that for cross reference each of the points are corresponding to the points in the initial test file, i.e. the first point of the reduced file corresponds to the first point in the test file and so on. This can be useful when there is more information in the data file that was not run through MultiProbe. Thus the results from MultiProbe can be matched with the original data point by point. The format of the output file allows for easy interfacing with graphing and data analysis tools like TecPlot, Excel etc. For quick viewing of the data reduction results the graphing tool included with MultiProbe can be used. See Analyzing Reduced Data.



## ANALYZING REDUCED DATA

### *View | MultiGrapher*

MultiProbe features a simple graphing program that can upload any space delimited text file given a few conditions; the file must be in columns and must have one (1) line of header describing what is in the individual columns. The output file from MultiProbe can be directly uploaded into this grapher.

1. Load the data file. Make sure that it is a valid data format of the file (see above), by pressing **Load**.
2. Select the y- and x-axis data from the two combo boxes.
3. Press **Update** to update the plot.

## CALLING MULTIPROBE DATA REDUCTION FROM CUSTOM APPLICATIONS

MultiProbe can be called from any other modern programming language as a dynamic-link library or dll. The program that needs to be called is *LLS.dll*. It is important that a calibration file is first preprocessed using MultiProbe before using the dll. The dll can be incorporated into e.g. LabVIEW programs for online reduction of probe pressures. The dll only uses 5 inputs:

Input:

1. A preprocessed file. This file must include the full path if located in a different directory than *LLS.dll*.
2. The number of ports the probe has. (will be removed in a later version)
3. A pressure array containing either the 5 or 7 pressures. The ordering of these pressures is very important. Description will follow.
4. Reference pressure.
5. Total pressure.

Output: The dll will return a number of parameters:

1. Calculated angle 1.
2. Calculated angle 2.
3. Ptot.
4. Pstat.
5. Vmagn
6. U
7. V
8. W
9. Mach
10. Re
11. Rho
12. Viscosity
13. Enthalpy



The calling format is as follows:

*LLSReduction(ProbeBase.Files.ProcessedFileName,ProbeBase.Geometry.NumPorts,  
press,Pref,Ttot,cAng1,cAng2,Ptot,Pstat,Vmagn,u,v,w,Mach,Re,Ts,Rho,Visc,Enth);*

A more detailed description will follow.

## ***ANALYSIS OF PREPROCESSED CALIBRATION DATA***

Use **View | Calibration File** on the main menu.

### **Calibration File:**

#### **Step 1. Upload a data file.**

1. Upload a preprocessed calibration file. (Typically \*.mpr)

#### **Step 2. Analysis of the calibration file.**

1. Scroll through the calibration file point by point and read on the screen all the information that is provided about that particular point.
2. View the port pressures as defined in the default (internal algorithm) definition. See appendix. A. Definitions.
3. Plot any information provided in the drop down menus on either y- or x-axis.
4. Mark which y axis you want to include on the plot.
5. Note that you can left-click the mouse and drag right for zooming a window or dragging left to undo the zoom. You can right-click the mouse and pan the window.

#### **ProbeBase: View the information that is entered in the probe database.**

This information can be useful for troubleshooting. All of the information available to MultiProbe during data analysis is displayed here.

## ***UNCERTAINTY ANALYSIS***

Online uncertainty analysis will be implemented.

## ***SPECIFICATIONS***

### **Specifications | Surface Fits**

Change the data reduction parameters

### **Specifications | LLS Library**

Set the specifications for the DLL operation

## **APPENDIX A. PORT NUMBERING DEFINITIONS**

*See also Help | Definitions on the main menu.*



### ***Port Numbering***

Port orientations used internally by the algorithm. Will be referred to as **standard port numbering**.

For 5-hole probes (figure XX).

For 7-hole probes (figure XX).

## ***APPENDIX B. PRESSURE MEASUREMENTS***

MultiProbe accepts a wide range of different pressure configurations. Typically calibrations and experiments are never setup in the same manner, thus MultiProbe can accept most typical configurations to successfully reduce the data from almost any experiment.

There are a wide range of available pressure transducers but they can be generalized into two main groups; absolute and differential pressure transducers. Their individual advantages and disadvantages will not be discussed here; rather the individual applications of the two for pressure probes. When using differential pressure measurements there is always a (reference) pressure that the pressure is differential with respect to. This pressure is often the atmospheric pressure, but can also be the static pressure of the system. Thus MultiProbe accepts that both the calibration total and port pressures can be differential w.r.t. the static pressure. See table 1 for all possible configurations.

**Table 1. Possible pressure configurations in MultiProbe.**

	Absolute	Differential w.r.t. Reference Pressure	Differential w.r.t. Static Pressure	Other (calibration curve input)
Reference Pressure	Yes*	-	-	-
Static Pressure	Yes	Yes**	-	-
Total Pressure	Yes	Yes**	Yes***	-
Port Pressure	Yes	Yes**	Yes***	Yes

\*Not required if all other pressures are absolute or static pressure is absolute and other pressures are w.r.t. the static pressure.

\*\*Reference pressure must be available.

\*\*\*Static pressure must be available (either absolute or differential w.r.t. reference pressure).

MultiProbe works internally with absolute pressure measurements. This means that if differential pressure transducers are being used, a reference pressure measurement must be provided. This measurement can either be provided in calibration or test file or manually. Required pressures for **calibration** of the probe are static and total pressure, the 5 or 7 port pressures. If any of the pressures are differential with respect to the reference pressure this pressure must also be provided. Required pressures for **test data** using a calibrated probe are the 5 or 7 port pressures and a reference pressure. The reference pressure of the transducer must be absolute.



## APPENDIX C. ANGLE DEFINITIONS

This version of MultiProbe does not manipulate angles. Angles are referred to as angle 1 and angle 2 and are generic angles. E.g. is cone and roll angles are entered (as for standard AeroProbe file format) the calculated angles that is reported by MultiProbe will be Angle 1 = Cone and Angle 2 = Roll.) Since this version does not use any manipulation of the angles the velocity components of the velocity magnitude are not calculated.

## APPENDIX D. COEFFICIENT DEFINITIONS

### Part 1. Calibration

- 1) When main sector is center port:
  - a) Calculate:  $b_1^1$  and  $b_2^1$
  - b) Calculate:  $b_1^i$  and  $b_2^i$ : where  $i=2..7$
  - c) Calculate:  $Atla^1$  and  $Asla^1$
  - d) Calculate:  $Atha^i$  and  $Asha^i$ : where  $i=2..7$
- 2) When main sector is any of the circumferential ports:
  - a) Calculate:  $b_1^i$  and  $b_2^i$ : where  $i=\max p1$
  - b) Calculate:  $b_1^{i-1}$  and  $b_2^{i-1}$ : where  $i=\max p1$  (CCW)
  - c) Calculate:  $b_1^{i+1}$  and  $b_2^{i+1}$ : where  $i=\max p1$  (CW)
  - d) Calculate:  $b_1^1$  and  $b_2^1$
  - e) Calculate:  $Atha^i$  and  $Asha^i$ : where  $i=\max p1$
  - f) Calculate:  $Atha^{i-1}$  and  $Asha^{i-1}$ : where  $i=\max p1$  (CCW)
  - g) Calculate:  $Atha^{i+1}$  and  $Asha^{i+1}$ : where  $i=\max p1$  (CW)
  - h) Calculate:  $Atla^1$  and  $Asla^1$

### Part 2. Data Reduction (search)

- 1) Calculate:  $b_1^i$  and  $b_2^i$  where  $i=\max p1$
- 2) Search Main Region
  - a) Search database where  $\max p1_T = \max p1_C$
  - b) From this region assign:
    - i) Angle 1 and angle 2
    - ii)  $b_1^i$  and  $b_2^i$  where  $i=\max p1$
    - iii)  $Atx^i$  and  $Asx^i$  where  $i=\max p1$
- 3) Search 2<sup>nd</sup> closest region
  - a) Search database where  $\max p2_T = \max p1_C$  AND  $\max p1_T = \max p2_C$  (to reduce number of points)
  - b) If  $\max p1_T = 1$  (main region is center region) assign:
    - i) Angle 1 and Angle 2
    - ii)  $b_1^1$  and  $b_2^1$  (i.e. use the centerport definitions of the circumferential points)
    - iii)  $Atla^1$  and  $Asla^1$
  - c) If  $\max p1_T > 1$  (main region is circumferential region) assign:
    - i) Angle 1 and Angle 2



- ii) If  $\max p_{2T}=1$  (also  $\max p_{1C}$ ) then:
    - (1)  $b_1^i$  and  $b_2^i$  where  $i=\max p_{1T}$
    - (2)  $A_{th}^i$  and  $A_{sh}^i$  where  $i=\max p_{1T}$
  - iii) If  $\max p_{2T}=\text{CCW}(\max p_{2T})$  then
    - (1)  $b_1^{i-1}$  and  $b_2^{i-1}$  where  $i=\max p_{1T}$
    - (2)  $A_{th}^{i-1}$  and  $A_{sh}^{i-1}$  where  $i=\max p_{1T}$
  - iv) If  $\max p_{2T}=\text{CW}(\max p_{2T})$  then
    - (1)  $b_1^{i+1}$  and  $b_2^{i+1}$  where  $i=\max p_{1T}$
    - (2)  $A_{th}^{i+1}$  and  $A_{sh}^{i+1}$  where  $i=\max p_{1T}$
- 4) Search 3<sup>rd</sup> closest region
- a) Search database where  $\max p_{3T}=\max p_{1C}$  AND  $\max p_{2T}=\max p_{2C}$  AND  $\max p_{1T}=\max p_{3C}$  (to reduce number of points)
  - b) If  $\max p_{1T}=1$  (main region is center region) assign:
    - i) Angle 1 and Angle 2
    - ii)  $b_1^1$  and  $b_2^1$  (i.e. use the centerport definitions of the circumferential points)
    - iii)  $A_{tl}^1$  and  $A_{sl}^1$
  - c) If  $\max p_{1T}>1$  (main region is circumferential region) assign:
    - i) Angle 1 and Angle 2
    - ii) If  $\max p_{3T}=1$  (also  $\max p_{1C}$ ) then:
      - (1)  $b_1^i$  and  $b_2^i$  where  $i=\max p_{1T}$
      - (2)  $A_{th}^i$  and  $A_{sh}^i$  where  $i=\max p_{1T}$
    - iii) If  $\max p_{3T}=\text{CCW}(\max p_{3T})$  then
      - (1)  $b_1^{i-1}$  and  $b_2^{i-1}$  where  $i=\max p_{1T}$
      - (2)  $A_{th}^{i-1}$  and  $A_{sh}^{i-1}$  where  $i=\max p_{1T}$
    - iv) If  $\max p_{3T}=\text{CW}(\max p_{3T})$  then
      - (1)  $b_1^{i+1}$  and  $b_2^{i+1}$  where  $i=\max p_{1T}$
      - (2)  $A_{th}^{i+1}$  and  $A_{sh}^{i+1}$  where  $i=\max p_{1T}$

